Super-resolved digital terrain models for GEDI geolocation correction: agreement with airborne LiDAR DTM-based corrections at the beam level, not the footprint level

Natsuki Yuda[1], Shinichiro Shirota[1,*]

[1]Hitotsubashi University, 2-1 Naka, Kunitachi, Tokyo 186-8601, Japan

[*]Corresponding author: shinichiro.shirota@r.hit-u.ac.jp (N. Yuda: dm250019@g.hit-u.ac.jp)

arXiv:2611.09854v1 [eess.IV] 6 Nov 2026

Abstract The Global Ecosystem Dynamics Investigation (GEDI) mission measures three-dimensional forest structure with a LiDAR aboard the International Space Station. GEDI observations have geolocation errors of about 10 m, which cause misalignment with other remote sensing data and reduce the accuracy of downstream tasks. Matching GEDI ground elevations against high-resolution digital terrain models (DTMs) from airborne LiDAR is one way to correct these errors, but such DTMs exist in few regions. To widen this method's applicability, we super-resolved a more widely available low-resolution DTM and used it for the matching. Our question is whether a super-resolved DTM yields the same correction as a 1 m-resolution airborne LiDAR DTM and, if not, why. In steep forests of western Japan, we super-resolved an existing 10 m-resolution DTM to 1 m. Improving its accuracy required fusion with a global 30 m-resolution DTM from a different source. Using the resulting DTM, we corrected GEDI observation positions first by a single shift per ground track, then per observation. For most tracks, the shifts nearly matched those from the airborne LiDAR DTM, likely because DTM errors canceled out across many observations. Per-observation corrections, however, did not match. At a single observation, the error does not cancel out and is too large for the correction. This error likely originates mainly from the input DTM. Therefore, even without a 1 m-resolution DTM, a roughly 10 m-resolution DTM, fused with a global DTM and super-resolved to 1 m, should yield track-wise corrections nearly matching those from a 1 m-resolution DTM.

Keywords GEDI; geolocation error; digital terrain model; super-resolution

1 Introduction

The Global Ecosystem Dynamics Investigation (GEDI) is a LiDAR mission aboard the International Space Station designed to measure the three-dimensional structure of forests globally (Dubayah et al., 2020). GEDI collects observation data, including ground elevation and canopy height, for each laser-illuminated area (a footprint approximately 25 m in diameter) over forests between latitudes 51.6°N and 51.6°S. These data serve as the basis for a wide range of applications, including global canopy height mapping (Potapov et al., 2021; Lang et al., 2023) and aboveground biomass estimation (Dubayah et al., 2022), and contribute to understanding the structure of forest ecosystems and quantifying the carbon cycle.

GEDI footprints have a horizontal positional error known as geolocation error. In Version 2, available since 2021, the horizontal error is approximately 10 m at one standard deviation (Tang et al., 2023), and even for Version 3, released in 2026, the mean one-standard-deviation horizontal error is reported to be 9.5 m (Dubayah et al., 2026); this error causes spatial inconsistency between the observation positions reported by GEDI and the actual measurement positions, making it difficult to match GEDI data with field measurements or other remote sensing data (Tang et al., 2023). Furthermore, it has been reported that geolocation error increases the uncertainty in canopy height estimation and aboveground biomass estimation (Roy et al., 2021; Milenković et al., 2017), and that the effect of geolocation error is amplified in areas with topographic relief (Quiros et al., 2021; Cardenas-Martinez et al., 2025). Correction of geolocation error is therefore required to improve the quality of GEDI data and to enable applications at the scale of individual footprints.

Methods proposed for correcting geolocation error include a waveform matching method based on airborne LiDAR point cloud data (Hancock et al., 2019) and DTM-based methods, which compare high-resolution bare-earth elevation data (a digital terrain model, DTM) with the ground elevation observed by GEDI (Tang et al., 2023; Schleich et al., 2023; Li et al., 2025). The latter methods search for the horizontal position at which the difference between the ground elevation observed by GEDI and the elevation read from the high-resolution DTM is minimized, and regard that position as the true footprint position. Hereafter, we refer to the elevation data used for this matching as the reference DTM (also called the reference surface). These DTM-based methods are less affected by seasonal changes in vegetation because they refer to bare-earth elevation. They are also easier to apply over wider areas because they do not depend on airborne LiDAR point cloud data. Indeed, Li et al. (2025) corrected more than 2.7 million footprints in forests using a DTM of approximately 1 m resolution covering 153,670 km^2 of Japan as the reference surface, and showed that the relative RMSE of canopy height improved from 35.55% to 21.07% in comparison with the maximum canopy height derived from airborne LiDAR independently of the correction. However, all DTM-based methods require a DTM with a resolution finer than the magnitude of the geolocation error, and

This paper is licensed under CC BY 4.0, except for the images in Figures 4.1, 5.2, and 5.3 that are marked as derived from FABDEM, which are licensed under CC BY-NC-SA 4.0.

their applicability is restricted to the limited regions where high-resolution data have been produced. Correction using a globally available 30 m-resolution digital elevation model (DEM) as the reference surface has also been attempted (Tsutsumida et al., 2026), but whether a DEM whose grid spacing exceeds the magnitude of the geolocation error (approximately 10 m) can distinguish positional errors of that magnitude has not been verified.

Meanwhile, in the field of remote sensing, super-resolution, which estimates high-resolution elevation data from low-resolution elevation data, has been studied as a means of obtaining high-resolution elevation data, and deep learning-based methods in particular have been actively studied in recent years (Demiray et al., 2021; Zhang et al., 2022; Helmy et al., 2026). In particular, Helmy et al. (2026) achieved super-resolution from a 10 m-resolution DTM to 1 m resolution, a result suggesting that surface generation by super-resolution could overcome the constraint on geolocation correction imposed by the scarcity of high-resolution DTMs. However, a DTM generated by super-resolution contains errors at various scales of the terrain. Because geolocation correction determines the position by matching the elevation of the reference surface against the observed ground elevation, the reference-surface error directly affects the correction results. The question of this study is therefore whether a generated reference surface that contains errors gives the same correction results as when a measured 1 m-resolution DTM is used as the reference surface, and if not, why not.

In this study, we propose a method that integrates super-resolution of DTMs with GEDI geolocation correction in order to extend geolocation correction to regions where no high-resolution DTM has been produced. The goal is to approximately reproduce, in regions where such data do not exist, the correction results that would be obtained if a 1 m-resolution DTM were available. A 10× super-resolution model is trained using the 10 m-resolution and 1 m-resolution DTMs published by the Geospatial Information Authority of Japan (GSI). These data represent the bare-earth elevation of the same area, but were produced independently by different measurement methods, namely airborne LiDAR and topographic map contour lines. In addition to the 10 m-resolution DTM, the super-resolution model uses a global 30 m-resolution DTM from which forest and building heights have been removed (FABDEM) as an auxiliary input, and extracts the features of both through intermediate fusion (mid-fusion). Using the generated high-resolution DTM as the reference surface, the systematic error of each beam and the individual error of each footprint are corrected in stages. For the footprint-level search, flow accumulation is adopted with the aim of being less susceptible to the instability of a solution determined by the single point of minimum cost, and its results are compared with those of grid search. The correction results are compared on a common set from which footprints that reached the boundary of the search range were excluded as correction failures.

As an example of forested areas, the evaluation is carried out in forested areas of western Japan where a 1 m-resolution DTM has been produced. Approximately 330,000 GEDI footprints in 10 test blocks that were not used for training the super-resolution model are the targets of correction. In this study, the 1 m-resolution DTM is regarded as the true terrain. It is at once the training target for super-resolution, one of the bases for evaluating the correction, and the basis for defining the reference-surface error. Furthermore, a correction that directly uses the same 1 m-resolution DTM as the reference surface, that is, a correction under the same conditions as the existing methods, is performed within the same framework and serves as the benchmark for comparing the correction results. This benchmark is itself an estimated corrected position, not the true horizontal position. The effect of the reference surface is examined by the agreement between the corrected positions of the two and by checking the relationship that holds when the footprint-level correction works as expected. In addition, both are evaluated by the ground elevation after correction and by the canopy height referenced to an airborne LiDAR-derived canopy height model obtained independently of the reference surface. Validation data for canopy height are available in some of the 10 test blocks.

The contributions of this study are as follows. First, as the first attempt to apply a DTM generated by super-resolution to geolocation correction, we propose a framework that integrates super-resolution and geolocation correction, and show its potential to extend GEDI geolocation correction beyond the regions where high-resolution DTMs have been produced, to which it has so far been limited. Second, we show that a reference surface obtained by super-resolution from an existing, publicly available low-resolution DTM and an auxiliary DTM gives nearly the same offsets as the 1 m-resolution DTM in the beam-level correction, whereas in the footprint-level correction the reference-surface error shifts the corrected positions, and we derive the reference-surface accuracy required for the footprint-level correction as a relationship between the reference-surface error and the elevation difference that the correction attempts to resolve. Third, we show that most of the reference-surface error consists of components at scales that can be represented by the 10 m-resolution DTM, and, since this error is considered to originate mainly from the input, argue that super-resolution useful for geolocation correction requires reducing the error of the input DTM.

The main results obtained in this study are as follows. The trained super-resolution model achieved an RMSE of 3.80 m in the evaluation against the 1 m-resolution DTM, which is 33.9% lower than the 5.74 m of bilinear interpolation, and reduced the vertical bias from 1.61 m to 0.10 m. The beam-level correction with this reference surface gave offsets close to those of the correction with the 1 m-resolution DTM, and the degree of agreement increased with the number of footprints in a beam. The mean absolute error (MAE) of canopy height after correction through the footprint-level stage was 5.24 m with the generated reference surface and 5.02 m with the 1 m-resolution DTM, a difference of only 0.22 m, or 0.11 m on the common set of footprints evalu-

ated in both. In contrast, the corrected positions of the footprint-level correction differed between the two, and the ground-elevation MAE of 2.6 m for the correction with the generated reference surface coincided with the reference-surface error at the corrected positions. This is because the reference-surface error was comparable to the elevation difference that the footprint-level correction attempts to resolve; when the model was trained with inputs synthesized from the 1 m-resolution DTM, the corrected positions also agreed. It was found that the generated reference surface can substitute for the 1 m-resolution DTM in the beam-level correction, whereas in the footprint-level correction its error shifts the corrected positions. As the method for the footprint-level correction, flow accumulation is recommended on the basis of the canopy height evaluation and the agreement with the corrected positions obtained with the 1 m-resolution DTM. Most of the reference-surface error consists of components at scales that can be represented by the 10 m-resolution DTM and that remain even after averaging with a Gaussian window, and is considered to originate mainly from errors originally present in the input.

2 Related work

2.1 GEDI geolocation correction

GEDI footprints contain horizontal geolocation errors, which directly affect the accuracy of the data products. These geolocation errors arise from multiple factors, including the pointing accuracy of the lasers, the accuracy of the position and attitude of the International Space Station, and the accuracy of the ranging and time-tag corrections.

Several studies have quantitatively evaluated the magnitude of the geolocation errors. Although the design specification of GEDI gives a horizontal geolocation accuracy within 10 m at one standard deviation (Dubayah et al., 2020), Yang et al. (2024) reported that, in northeastern China, the standard deviation of the geolocation deviations of individual footprints was approximately 15 m, exceeding the nominal value. Shannon et al. (2024) estimated the systematic geolocation error to be 9.62 m (toward the southwest) using a Bayesian model and showed that the probability that the true footprint center lies within 20 m of the reported position is only approximately 45%. Quiros et al. (2021) conducted a comprehensive accuracy assessment of 12,031 footprints in southwestern Spain and confirmed that moving the footprints by 10 m in the 270-degree direction reduced the ground elevation error the most. Tang et al. (2023) reported that 22.7% of the beams in the GEDI Release 1 data had systematic errors exceeding 25 m, whereas in Release 2, 80.8% of the beams had systematic errors of less than 10 m.

The influence of geolocation errors on downstream data products has also been evaluated. Roy et al. (2021) simulated GEDI waveforms from airborne LiDAR in a secondary tropical forest in the Democratic Republic of the Congo and performed Monte Carlo simulations in which the footprint center was moved 300 times according to the GEDI geolocation error (mean 0 m, standard deviation 10 m). The interquartile range of the simulated relative height RH95 varied among footprints from 0.02 m to 17.98 m and was larger in spatially heterogeneous canopies containing small stands, canopy gaps, and forest edges. Milenković et al. (2017) simulated spaceborne LiDAR from airborne LiDAR data and showed that a geolocation error of 14 m increases the variance of aboveground biomass estimates by 17%. Quiros et al. (2021) and Cardenas-Martinez et al. (2025) reported that the influence of geolocation errors is further amplified in areas with steep slopes.

Methods for correcting geolocation errors are broadly classified into two categories according to the type of reference data used. **Waveform matching-based methods** simulate waveforms that mimic the observation conditions of GEDI from dense airborne LiDAR point clouds and search for the position at which the similarity to the observed waveform is maximized. Hancock et al. (2019) developed and validated a GEDI waveform simulator. They compared waveforms simulated from co-registered airborne LiDAR point clouds with measured waveforms of the Land, Vegetation, and Ice Sensor (LVIS) and confirmed that the differences in the **relative height percentiles (RH metrics)** above the ground had a bias of less than 0.22 m and a root mean square error (RMSE) of less than 5.7 m. This simulator has become the foundation of subsequent waveform matching studies. Xu et al. (2023) performed waveform matching at eight sites in the United States using this simulator and detected geolocation errors of 20.91 m on average. However, their method corrects only the systematic error common to an entire beam and does not address the random error of each footprint. Mkaouar et al. (2025) proposed a method using physically based radiative transfer simulation with the Discrete Anisotropic Radiative Transfer (DART) model and achieved a high degree of agreement with the observed waveforms, with coefficients of determination of 0.94 to 0.99. However, this method has the limitations of high computational cost and difficulty in identifying the position in uniform dense forests. Wang et al. (2025) proposed a Monte Carlo method that randomly moves the footprint positions using the agreement with canopy height metrics derived from airborne LiDAR as the criterion. Corado et al. (2026) released GEDI-Correct, a Python tool that performs matching at three levels, namely orbit, beam, and footprint, against any one of waveforms, RH distributions, or ground elevations simulated from airborne LiDAR point clouds. The idea of separating the levels of correction is close to the beam-level and footprint-level corrections of this study; however, their footprint-level correction determines a common offset for a group of approximately 8–10 temporally consecutive footprints and applies it to the central footprint, which differs from the footprint-level correction of this study, in which the offset is determined from a single footprint alone. All of these methods have in common that they require airborne LiDAR point clouds.

DTM-based methods compare a high-resolution DTM with the ground elevation observed by GEDI and

search for the position at which the elevation difference is minimized (Tang et al., 2023; Schleich et al., 2023; Li et al., 2025; Tsutsumida et al., 2026). Tang et al. (2023) detected and corrected the systematic geolocation error of each beam using a 1 m resolution bare-earth elevation model obtained from the 3D Elevation Program (3DEP) of the United States as the reference surface. They adopted a scheme that weights the elevations within a footprint with a Gaussian distribution and applies the correction as a constant offset per beam. Schleich et al. (2023) developed the GeoGEDI method using a 1 m resolution digital elevation model (DEM) of France and performed a correction that aggregates neighboring footprints into clusters. The GeoGEDI method is characterized by determining the optimal corrected position using flow accumulation, which achieves a more robust correction than a simple minimum search. Li et al. (2025) performed a point-level correction, in which more than 2.7 million footprints were corrected footprint by footprint, using a DTM of Japan with approximately 1 m resolution. The point-level correction reduced the RMSE of the ground elevation from 18.42 m to 2.67 m and the relative RMSE of the canopy height from 35.55% to 21.07%. Tsutsumida et al. (2026) proposed SALPA, which replaces the exhaustive search over candidate points on a grid with continuous optimization (L-BFGS-B, a genetic algorithm, particle swarm optimization, and the whale optimization algorithm), and reported that, with 0.5–1 m resolution DEMs derived from airborne LiDAR in Nikko, Japan, and the Landes region of France as the reference surfaces, the elevation difference between the GEDI ground elevation and the reference surface became slightly smaller than with the GeoGEDI method. They also showed that the computation runs with AW3D30, a global 30 m resolution digital surface model (DSM), as the reference surface, pointing toward correction with globally available elevation data alone. However, the evaluation was based on the elevation difference from the DEM used for the correction, and the authors themselves state that the extent to which the reduction in the elevation difference corresponds to the correction of geolocation errors requires further verification. Whether a DEM with 30 m grid spacing can resolve the approximately 10 m geolocation error of GEDI has not yet been verified.

DTM-based methods have the following advantages over waveform matching methods. First, they do not require dense airborne LiDAR point cloud data of vegetation and can be applied over wider areas wherever a DTM is available. Second, because a DTM represents the bare-earth elevation, it is temporally stable and can be used as the reference surface even when its acquisition time differs from that of GEDI. This contrasts with vegetation data, which depend strongly on seasonal changes. On the other hand, major challenges include the following: the applicable range is limited to areas where a high-resolution DTM is available; in areas with little relief, the sensitivity of the objective function decreases, making it difficult to identify the optimal position (Tang et al., 2023; Tsutsumida et al., 2026); and, when the optimal position is searched for footprint by footprint, the correction may fit local elevation variations of the reference DTM and exceed the true geolocation error (Li et al., 2025).

2.2 Super-resolution

2.2.1 Super-resolution in computer vision

The super-resolution techniques used to enhance the resolution of DTMs and DEMs are based on image super-resolution methods developed in the field of computer vision. Image super-resolution is an inverse problem of estimating a high-resolution image from a low-resolution image, and it has developed rapidly since the introduction of deep learning.

A variety of architectures have been proposed as deep learning models for super-resolution. SRCNN by Dong et al. (2016) was a pioneering work on super-resolution with convolutional neural networks, and Ledig et al. (2017) introduced generative adversarial networks (GANs) into super-resolution with SRGAN and proposed a method that generates perceptually natural images. Methods that exploit deep residual learning have also been developed; Lim et al. (2017) proposed EDSR, an efficient residual network without batch normalization. RCAN (Residual Channel Attention Network) by Zhang et al. (2018) is a model that combines a Residual in Residual structure, which nests residual structures within a residual structure, with a channel attention mechanism that adjusts the importance of each channel through learning. By adaptively attending to informative feature channels through the channel attention mechanism, it achieves higher accuracy in restoring high-frequency components than a simple residual network.

2.2.2 Super-resolution of DTMs and DEMs

In applying super-resolution architectures from the computer vision field to DTMs and DEMs, models and loss functions have been designed with consideration of the differences in properties from natural images. Whereas the perceptual quality of textures is emphasized in the super-resolution of natural images, numerical accuracy of elevation values is required for DTMs. Moreover, because mean squared error or L1 loss alone does not sufficiently preserve topographic features such as slopes, ridges, and valley lines, the design of loss functions suited to terrain data has become an important research topic.

Over the past few years, a variety of deep learning approaches have been proposed for the super-resolution of DTMs/DEMs. Among GAN-based methods, Demiray et al. (2021) performed approximately 16.7× super-resolution from approximately 15 m resolution to approximately 0.9 m resolution with D-SRGAN, which is based on the SRGAN architecture. Among convolutional neural network-based methods, Zhang et al. (2022) proposed TfaSR, which combines deformable convolution with a cooperative loss function that takes terrain features into account (elevation loss, slope loss, and watershed-neighborhood loss), and performed super-resolution from 30 m resolution to 10 m resolution. Among residual network-based methods, Helmy et al. (2026) modified

RCAN to perform 10× super-resolution from 10 m resolution to 1 m resolution and showed that the combination of L1 loss and slope loss gives the best results. Among Transformer-based methods, Zheng et al. (2024) proposed TUGAN, which uses a self-similarity Transformer as the generator and a U-Net as the discriminator. In addition, Liu et al. (2026) performed super-resolution of up to 16× with GSRMTL, a multi-task learning method that uses high-resolution optical images as guidance and jointly learns DEM super-resolution and semantic segmentation, and Yu et al. (2025) proposed DSRFlow, which is based on normalizing flows.

In studies comparing GAN-based methods with non-GAN-based methods for super-resolution at large upscaling factors of 4× or greater, many have reported a tendency for the GAN-based methods to be inferior in elevation accuracy (Zhang et al., 2022; Li et al., 2023; Zheng et al., 2023; Wang et al., 2024). Although results in which GAN-based methods outperform some non-GAN-based methods have also been reported (Demiray et al., 2021; Liu et al., 2026), no result has shown a clear advantage over non-GAN-based methods in general. It should be noted that none of these existing studies aimed at a fair comparison of methods and that, to our knowledge, no comprehensive comparative study exists. Nevertheless, the fact that a consistent tendency has been observed across multiple independent studies suggests that GAN-based methods tend to be at a disadvantage in elevation accuracy for super-resolution with large upscaling factors. One reason behind this is that GANs are designed to optimize perceptual quality and prioritize the naturalness of textures over the numerical accuracy of elevation values, so that texture hallucination and checkerboard artifacts tend to occur (Wu et al., 2021). In the super-resolution of DTMs, the numerical accuracy of elevation is the most important, and these side effects accompanying the optimization of perceptual quality directly impair accuracy as topographic distortions. From the above, we consider that accuracy-oriented architectures are more suitable than GAN-based ones for the super-resolution of DTMs with large upscaling factors.

Finally, we mention the problem of training and evaluation data common to the super-resolution of DTMs/DEMs. The great majority of super-resolution studies construct their training and evaluation data by synthesizing low-resolution data through downsampling of high-resolution data (Helmy et al., 2026; Demiray et al., 2021; Zhang et al., 2022; Zheng et al., 2023; Li et al., 2023; Wang et al., 2024; Yu et al., 2025); studies of super-resolution using real DEM pairs are few (Wu et al., 2021; Zhang and Yu, 2022), and only recently have studies that handle real data pairs with optical images as auxiliary input begun to appear, such as one that guides a global DEM with aerial photographs to perform bare-earth conversion and resolution enhancement simultaneously (Cai and Wilson, 2025) and one that guides real data pairs of urban DSMs with optical images (Panangian and Bittner, 2024). The main reasons why synthetic data are widely used are that it is difficult to obtain real data pairs in which the same area is observed with different sensors at different resolutions, and that evaluation is easy with synthetic data because the high-resolution data themselves can be used as the ground truth.

However, Wu et al. (2021) pointed out a large gap between real data and synthetic data. They performed super-resolution with real-world data from the 30 m resolution data of the Shuttle Radar Topography Mission to the 10 m resolution data of WorldDEM and experimentally showed that a model trained on synthetic data does not generalize to real-world super-resolution tasks. As the cause, they cite that the relationship between a low-resolution DEM and a high-resolution DEM in the real world cannot be reproduced by simple downsampling because of differences in sensor characteristics, data acquisition time, and processing methods. Thus, from a practical standpoint, the need for training and evaluating models with real data pairs is strongly suggested.

3 Data

This study used the 1 m resolution DTM (DEM1A) and the 10 m resolution DTM (DEM10B) published by the Geospatial Information Authority of Japan (GSI), together with FABDEM, for super-resolution, and performed geolocation correction of the observation data of GEDI, a spaceborne LiDAR mission. In addition, the 50 m resolution JAXA High-Resolution Land Use and Land Cover map was used for land use and land cover classification in Japan, and the 0.5 m resolution DCHMs published by Hyogo Prefecture and Kochi Prefecture were used for evaluating canopy height estimates.

3.1 GEDI

The Global Ecosystem Dynamics Investigation (GEDI) is a full-waveform LiDAR mission aboard the International Space Station (ISS), designed to measure the three-dimensional structure of the Earth's forests at high resolution (Dubayah et al., 2020). GEDI was installed on the ISS in December 2018 and began observations in March 2019. Because of the orbital inclination of the ISS, GEDI observations are limited to latitudes between 51.6 degrees north and 51.6 degrees south. GEDI stopped observing in March 2023 and was stored on the ISS, but it was reinstalled in April 2024 and resumed observations in June of the same year.

The GEDI instrument carries three lasers with a wavelength of 1064 nm, which are optically dithered to produce eight ground tracks. The pulse repetition frequency of the lasers is 242 Hz, and each footprint is approximately 25 m in diameter. Footprints are spaced approximately 60 m apart along track, and the tracks are spaced approximately 600 m apart across track (Fig. 3.1). In GEDI, each of these eight ground tracks is called a beam and is identified by a name from BEAM0000 to BEAM1011. The four beams originating from the two high-output lasers are power beams (BEAM0101, 0110, 1000, 1011), and the four beams originating from the one laser whose output is split in two are coverage beams (BEAM0000, 0001, 0010, 0011) (Tang et al., 2023).

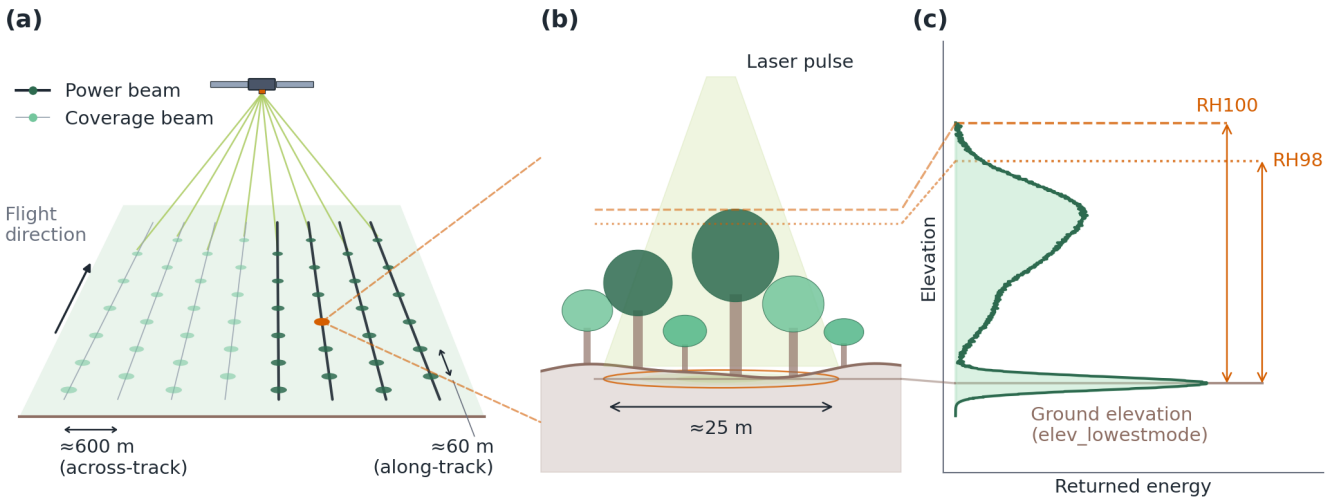


Fig. 3.1: Schematic of GEDI observations. (a) The eight beams emitted from the ISS and the ground tracks they form. Thick lines are power beams, which originate from the high-output lasers, and thin lines are coverage beams. (b) A laser pulse illuminating one footprint (approximately 25 m in diameter) and the canopy. (c) The relationship between the received waveform of a footprint and the ground elevation (the elevation of the lowest mode), RH98, and RH100 derived from it. RH98 and RH100 are heights above the ground elevation.

In this study, the term beam refers to the sequence of footprints aligned along one ground track of one orbit.

As a full-waveform LiDAR, GEDI records the entire reflected waveform of the laser pulse, so that the vertical structure of vegetation from the top of the canopy to the ground surface can be obtained in a single measurement. In particular, the **relative height percentiles** (RH) are metrics obtained by accumulating the energy of the received waveform from the bottom of the waveform and expressing the height at which the cumulative energy reaches a given fraction of the total energy as a height above the ground elevation (the elevation of the lowest mode); RH98 is the height at which 98% is reached. RH98 corresponds to the elevation near the canopy top minus the ground elevation, and is the measurement on which canopy height estimation by GEDI is based. The data products have been developed and released in stages, and this study used the Level 2A product, which contains the ground elevation and the relative heights of each footprint. We used Version 2 and targeted observations acquired from April 2019 through March 2023.

To ensure the reliability of elevation matching by excluding footprints with low waveform quality and those observed outside forests, we followed Li et al. (2025) and selected for geolocation correction the footprints that satisfied all of the following six conditions: (1) observed by a power beam; (2) beam sensitivity of at least 0.90; (3) valid waveform (l2_quality_flag = 1) that is not degraded (degrade_flag = 0); (4) observed at a site classified as forest in the JAXA High-Resolution Land Use and Land Cover map (v25.04); (5) RH98 of at least 5 m (following the forest definition of the Food and Agriculture Organization of the United Nations); and (6) if located at a site classified as deciduous forest in the same map, observed during the leaf-on period (day of year 120–270). For conditions (4) and (6), we used the version of the land use and land cover map closest to the observation year: the 2020 version for observations in 2019–2021 and the 2022 version for observations in 2022–2023. Furthermore, to exclude footprints of obviously poor quality, we added a condition not used by Li et al. (2025): (7) the absolute difference between the GEDI ground elevation and the DEM10B elevation is less than 60 m. Of the 2,114,311 footprints satisfying conditions (1)–(6), 0.61% (12,842 footprints) were excluded by condition (7).

3.2 DTM

A digital terrain model (DTM) is an elevation dataset representing the elevation of the bare ground surface, with features such as vegetation and buildings removed. In contrast, a digital surface model (DSM) represents the elevation of the entire surface, including the heights of vegetation and buildings (Farr et al., 2007; Hawker et al., 2022). Many studies on GEDI geolocation correction use DTMs, which do not include the effects of vegetation.

Few DTMs are available at the global scale. The Shuttle Radar Topography Mission (30 m; Farr et al., 2007) and Copernicus GLO-30 (30 m) are global elevation datasets acquired by interferometric synthetic aperture radar, but both are DSMs and include the heights of vegetation and buildings. FABDEM, described later, is a bare-earth DTM produced by removing the effects of vegetation and buildings from one of these DSMs, Copernicus GLO-30, and is freely available at 30 m resolution with global coverage (Hawker et al., 2022). Among commercial products, WorldDEM Neo DTM by Airbus provides a global DTM at 5 m resolution.

At the national or regional level, high-resolution DTMs have been published in some cases. GSI in Japan, the 3D Elevation Program (3DEP) in the United States, and the National Institute of Geographic and Forest Information (Institut national de l'information géographique et forestière) in France each provide DTMs at 1 m resolution. In this study, the DTMs published by GSI were used as the training target for super-resolution and as

the reference data for geolocation correction.

All three DTMs used in this study are grids aligned with latitude and longitude, and their grid spacings are defined exactly in arcseconds. The grid spacing is 0.04 arcseconds for DEM1A, 0.4 arcseconds for DEM10B, and 1 arcsecond for FABDEM. In our implementation, these grids are handled with integer coordinates in units of 0.04 arcseconds. When a grid spacing defined in arcseconds is converted to distance, it is nearly constant in the north–south direction, whereas in the east–west direction it becomes shorter at higher latitudes. Table 3.1 shows these distances in the study area (30 to 36 degrees north) together with the production method of each DTM.

As an example of a region where forests extend over steep mountains, this study targeted the forested areas of western Japan from 30 to 36 degrees north and from 128 to 135 degrees east. The main reasons for choosing this area are that few of its forests are covered with snow in winter and that the proportion of deciduous forest is small. The study area was divided into equal-sized blocks, 10 of which were designated as test blocks for evaluating super-resolution and geolocation correction, and the remaining area, excluding the buffers around the test blocks, was used for training and validating the super-resolution model. Fig. 3.2 shows the arrangement of the patches used for training, validation, and testing. The selection of the test blocks and the definition of the patches are described in Section 5.1.1.

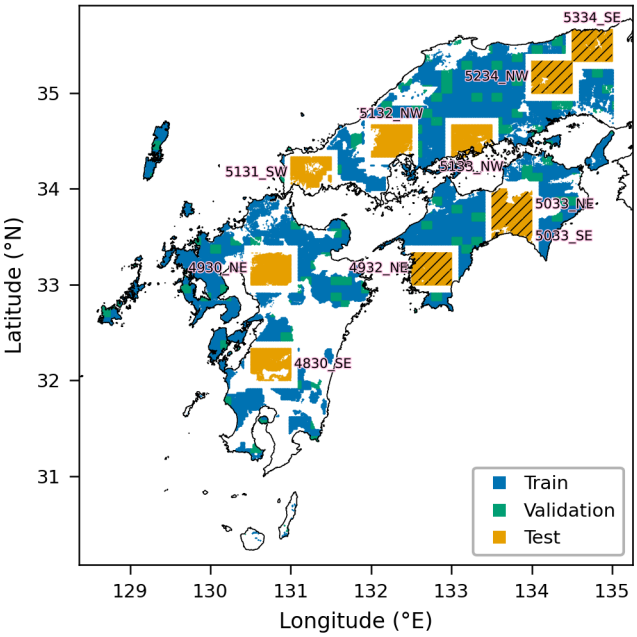


Fig. 3.2: Arrangement of the patches used as Train, Validation, and Test for the super-resolution model. The five test blocks for which DCHMs are available (5334_SE, 5234_NW, 5033_NE, 5033_SE, 4932_NE) are hatched. The hatched areas do not show the extents of the DCHMs themselves. The blank areas around the test blocks are buffers used for neither training nor validation.

3.2.1 DTMs of the Geospatial Information Authority of Japan (DEM1A, DEM10B)

GSI publishes several DTMs with different accuracies and resolutions, two of which were used in this study.

DEM1A is a DTM with approximately 1 m resolution (grid spacing 0.04 arcseconds) based on airborne LiDAR surveys. Its vertical accuracy is within 0.3 m (Li et al., 2025), and it is the high-accuracy dataset that this study used as the training target of the super-resolution model and for geolocation correction and its evaluation.

DEM10B is a DTM with 10 m resolution (grid spacing 0.4 arcseconds), produced from the contour lines of topographic maps. Its vertical accuracy, within 5 m, is lower than that of DEM1A, but DEM10B covers all of Japan and is available even in areas where DEM1A has not been produced. In this study, DEM10B was used as the input (low-resolution data) to the super-resolution model.

The elevations of DEM1A and DEM10B are orthometric heights referenced to the mean sea level of Tokyo Bay. Because GEDI elevations are recorded as ellipsoidal heights, we converted them to orthometric heights by subtracting the geoid height of GSIGEO2011 (Ver. 2.2). The elevations of FABDEM are heights above the EGM2008 geoid (Pavlis et al., 2012) and were used as input for super-resolution without conversion. Note that almost all of the DEM1A data obtained for this study are elevations after the height revision of April 2025 (JGD2024), whereas the elevations of DEM10B and GEDI are those before the revision (JGD2011). In the test blocks, the pre-revision elevations are higher by about 0.12 m on average, and results comparing DEM10B or GEDI elevations with DEM1A include this difference.

3.2.2 FABDEM

FABDEM (Forest And Buildings removed Copernicus DEM) is a global 30 m resolution DTM in which the heights of forests and buildings were removed from the Copernicus GLO-30 Digital Elevation Model by random forest regression (Hawker et al., 2022). FABDEM has been released as the first freely available global DTM at 30 m resolution with forest and building heights removed.

Because the source data, Copernicus GLO-30, is a DSM, its elevation values include the heights of vegetation and buildings, whereas FABDEM estimates and removes these heights with a random forest regression model. In an accuracy assessment over 12 evaluation areas worldwide, the mean absolute error in forested areas decreased from 5.15 m for Copernicus GLO-30 to 2.88 m, and that in urban areas from 1.61 m to 1.12 m (Hawker et al., 2022). The horizontal accuracy is inherited from Copernicus GLO-30 and is approximately 4 m.

In this study, FABDEM was used as input data for the super-resolution model. Because FABDEM was generated from a data source different from that of the 10 m resolution DTM of GSI (DEM10B), combining the two is expected to reduce bias. However, the mean absolute error of FABDEM in forested areas, 2.88 m, is still large, and its spatial resolution is limited to 30 m, so it is not suitable for geolocation correction on its own.

Table 3.1: Grid spacing and production method of the DTMs used in this study.

DTM	Grid spacing (arcsec)	North–south spacing (m)	East–west spacing (m)	Production method
DEM1A	0.04	approx. 1.23	approx. 1.00–1.07	Airborne LiDAR survey
DEM10B	0.4	approx. 12.3	approx. 10.0–10.7	Contour lines of topographic maps
FABDEM	1	approx. 30.8	approx. 25.0–26.8	Removal of forest and building heights from Copernicus GLO-30

3.2.3 Terrain roughness

Many studies have quantified and applied terrain roughness (surface roughness) using DTMs or digital elevation models (DEMs), but there is no single definition. Grohmann et al. (2011) defined it as "the variability of a topographic surface at a given scale" and compared six indices derived from elevation, slope, and curvature. Some indices measure local unevenness, others the relief of the whole area, and others the variability of slope, and which is appropriate depends on the purpose. For example, whether a uniformly inclined slope counts as rough differs among indices. Moreover, even for the same index, the value changes greatly with the resolution of the source data and the size of the area over which values are aggregated into a single value. Grohmann et al. (2011) demonstrated this with combinations of five resolutions and 12 window sizes. When comparing roughness, it is therefore necessary to match not only the definition of the index but also the resolution of the data and the size of the area over which the value is aggregated.

In this study, among the indices of Grohmann et al. (2011), we used the standard deviation of residual topography ($\mathrm{SD}_{\mathrm{restopo}}$) to examine the effect of terrain on super-resolution. Specifically, the terrain roughness of a patch of 500×500 pixels is defined for the 1 m resolution DTM as follows. Let z_i be the elevations of the valid pixels contained in the region Ω, and N their number. The standard deviation of residual topography is the standard deviation of the residuals obtained by subtracting a smoothed surface from the elevations. Let W_i be the 11×11 pixel window centered on pixel i and s_i the mean of the valid pixels within it; the smoothed surface is then given by

$$s_i = \frac{1}{|W_i|} \sum_{j \in W_i} z_j \tag{3.1}$$

Let the residual be $r_i = z_i - s_i$ and the mean of r within the region be μ_r; the standard deviation of residual topography is then defined as

$$\mathrm{SD}_{\mathrm{restopo}} = \sqrt{\frac{1}{N} \sum_{i \in \Omega} (r_i - \mu_r)^2} \tag{3.2}$$

There are two reasons for choosing this index. First, for $\mathrm{SD}_{\mathrm{restopo}}$, the residual is zero on a uniformly inclined slope, which is therefore not counted as roughness. This property is desirable because what this study focuses on is the fine unevenness that does not appear in the 10 m resolution DTM, not the inclination of the slope itself. Second, its values are in meters, so they can be compared side by side with super-resolution errors in the same unit.

The smoothing window was set to 11×11 pixels because this size is almost the same as the area covered by one pixel of the 10 m resolution DTM given as input. The residual then corresponds to the component that is not contained in the input and must be newly created by super-resolution. Grohmann et al. (2011) used the same size for the smoothing window and the aggregation area, whereas in this study the smoothing window is fixed at these 11×11 pixels and decoupled from the aggregation area (the patch of 500×500 pixels).

3.3 DCHM

A digital canopy height model (DCHM) is a raster dataset representing the height of vegetation at each grid point, obtained by subtracting a DTM from a DSM. In this study, 0.5 m resolution DCHMs produced by Japanese local governments from airborne LiDAR surveys were used as the data for evaluating whether geolocation correction improves the accuracy of canopy height estimation.

The DCHMs used in this study are those published by Hyogo Prefecture and Kochi Prefecture through the G-Spatial Information Center. The Hyogo Prefecture DCHM was produced from airborne LiDAR survey data acquired by Hyogo Prefecture in fiscal years 2020–2021, and overlaps two test blocks (5334_SE, 5234_NW). The same data also include the southeastern part of the prefecture surveyed by the Rokko Sabo Office of the Kinki Regional Development Bureau, Ministry of Land, Infrastructure, Transport and Tourism, in fiscal years 2012–2013, but this part was not used because it does not overlap any test block. The Kochi Prefecture DCHM was produced by Kochi Prefecture from airborne LiDAR survey data acquired by the Forestry Agency of Japan in fiscal year 2018, and overlaps three test blocks (5033_NE, 5033_SE, 4932_NE). Relative to the GEDI observation period (April 2019 through March 2023), the Kochi Prefecture DCHM was surveyed before it and the Hyogo Prefecture DCHM during it, and forest growth or logging that occurred during these time gaps can be a source of error in the comparison between the DCHMs and GEDI RH98.

4 Methods

This section describes the methods of this study. It consists of two parts. The first part describes the super-resolution method that generates a 1 m resolution DTM from a low-resolution DTM. The second part describes the method for correcting the horizontal geolocation error of GEDI footprints with the generated DTM.

In what follows, the methods are described by the roles that the data play rather than by the names of

individual datasets. Super-resolution uses one or more low-resolution DTMs as inputs and a high-resolution DTM as the training target. When there are multiple input DTMs, we call the one with relatively higher resolution and more data the primary input and the others auxiliary DTMs. Of the data described in the Data section, this study uses DEM10B as the primary input, FABDEM as the auxiliary DTM, and DEM1A as the high-resolution DTM. The reasons for incorporating the auxiliary DTM and how it is handled are described in Section 4.1.2.

4.1 Super-resolution

As the super-resolution model, we adopt as a basis the Modified RCAN that Helmy et al. (2026) proposed for DTM super-resolution. There are two reasons for this choice. First, that paper deals with the same 10× super-resolution from 10 m to 1 m resolution as this study, and its configuration is one of the few whose effectiveness has been demonstrated for DTM super-resolution at large upscaling factors. Second, as described in the Related work section, an accuracy-oriented design that restores high-frequency components with residual structures and channel attention suits DTM super-resolution, which requires numerically accurate elevation values.

The configuration of Helmy et al. (2026) has three key points: (1) the residual-group structure of RCAN (Zhang et al., 2018) is replaced with a simple body of RCABs (Residual Channel Attention Blocks) connected in series; (2) reflect padding is used in all convolutions to suppress artifacts at tile boundaries; and (3) the 10× upscaling, which includes a non-integer step, is split into three stages of 2.5×, 2×, and 2× and performed by progressive upsampling (Progressive Upsampler), in which each stage consists of bilinear interpolation, convolution, and LeakyReLU.

The model of Helmy et al. (2026) takes a single low-resolution DTM as input and is trained and evaluated with low-resolution data synthesized from a high-resolution DTM. This study trains the model with a real DTM pair. Unlike low-resolution data synthesized from a high-resolution DTM, a real low-resolution DTM has errors that originate from its production method. To deal with these errors, this study adopts a model structure that can take multiple DTMs as input. In the following, we denote the primary low-resolution input DTM by z_{lr}, the auxiliary DTM resampled to the grid of the primary input by z_{aux}, and the high-resolution DTM of the training target by z, and their normalized versions by $\bar{z}_{lr}$, $\bar{z}_{aux}$, and Y. That is, z and $\hat{z}$ are elevations in meters, and Y and $\hat{Y}$ are elevations in normalized space. The changes and additions relative to Helmy et al. (2026) are three: normalization by the deviation from a base elevation and the Global skip (Section 4.1.1); an encoder for each DTM and mid-fusion to input the auxiliary DTM (Sections 4.1.2 and 4.1.3); and a masked loss and evaluation that exclude missing values (Section 4.1.4).

4.1.1 Normalization by the base elevation and Global skip

Unlike the pixel values of natural images, the elevation values of a DEM vary greatly in range from place to place. DEM super-resolution has therefore used methods that normalize the elevation values of each tile to a fixed range (Zhang and Yu, 2022; Zheng et al., 2024) and detrending, which takes as the learning target the residual after subtracting a terrain trend obtained by smoothing (Wang et al., 2024). This study follows the latter idea. A patch is divided into cells of 10×10 pixels of the primary input, and the mean of the primary input within each cell is taken as the base elevation z_b. Let $\tilde{z}_b$ be the base elevation expanded to the low-resolution grid by bilinear interpolation, and let $\hat{z}_b$ be $\tilde{z}_b$ further upsampled to the output grid by bilinear interpolation. The inputs and the training target are normalized to deviations from the base elevation: $\bar{z}_{lr} = (z_{lr} - \tilde{z}_b)/k$, $\bar{z}_{aux} = (z_{aux} - \tilde{z}_b)/k$, and $Y = (z - \hat{z}_b)/k$. The constant k is set to 50 (m) in this study. The base elevation z_b of this study is a terrain trend corresponding to the smoothed surface that Wang et al. (2024) obtained with a Gaussian filter. The auxiliary DTM may or may not be included in the computation of the base elevation; this study does not include it. The Global skip is a connection that enlarges the normalized primary input $\bar{z}_{lr}$ to the output resolution by bilinear interpolation U and adds it to the output of the network f, so that the network learns the residual (Kim et al., 2016). The network thus learns only the details that bilinear interpolation cannot represent. The prediction in normalized space, $\hat{Y}$, and the prediction in meters, $\hat{z}$, obtained by multiplying it by k and adding $\hat{z}_b$, are given by

$$\hat{Y} = f(\bar{z}_{lr}, \bar{z}_{aux}, T) + U(\bar{z}_{lr}) \tag{4.1}$$

$$\begin{aligned} \hat{z} &= k\,\hat{Y} + \hat{z}_b \\ &= k\left(f(\bar{z}_{lr}, \bar{z}_{aux}, T) + U(\bar{z}_{lr})\right) + \hat{z}_b \end{aligned} \tag{4.2}$$

4.1.2 Auxiliary DTM

The purpose of adding the auxiliary DTM to the input is to reduce the systematic error (bias) of the DTM generated by super-resolution. A low-resolution DTM has systematic errors that originate from its production method, and as long as a single low-resolution DTM is the only input, the model can learn these errors only from their correspondence with the training target. If another DTM produced from a data source different from that of the primary input is also given as input, the errors of the two DTMs can be expected to differ in nature and complement each other, and the model can cancel part of the systematic error by collating the two. We therefore require the auxiliary DTM to derive from a data source and a production process different from those of the primary input. However, whether the auxiliary DTM actually contributes to accuracy is not known in advance. An auxiliary DTM usually has a coarser resolution than the primary input and can have errors of several meters in forested areas. Its contribution is something to be verified by experiments that compare

models with and without the auxiliary DTM, not an assumption.

The auxiliary DTM is generally expected to have a grid spacing different from that of the primary input. Because mid-fusion concatenates the outputs of the two encoders along the channel dimension pixel by pixel, the grids of the two outputs must be aligned so that the two concatenated pixels refer to the same location on the ground. The auxiliary DTM is therefore resampled to the grid of the primary input by bilinear interpolation before it enters the encoder. In this resampling, missing points among the four neighbors used for bilinear interpolation are excluded, and the interpolated value is computed after renormalizing the weights of the remaining neighbors to sum to one. Because the reliability of an interpolated value decreases as fewer neighbors are valid, the sum of the interpolation weights of the valid neighbors (0 to 1) is attached to the auxiliary DTM as a confidence channel T, which tells the encoder how reliable the interpolated value of each pixel is. The encoders consist only of convolutions and output feature maps on the same grid as their inputs, so the outputs of the two encoders are also aligned with the grid of the primary input.

4.1.3 Model architecture

The overall architecture of the super-resolution model of this study is shown in Fig. 4.1. The number of channels and the activation function of each layer are given in Appendix B; here we describe the flow of processing. Except for the 1×1 convolutions in the channel attention, the convolutions are 3×3 and use reflect padding. The network f has two input streams, the normalized primary input $\bar{z}_{lr}$ and the normalized auxiliary DTM $\bar{z}_{aux}$ with the confidence channel T attached, both on the grid of the low-resolution DTM. The model of Helmy et al. (2026) has a single input and consists of a single path from the first convolution to the RCAB model, whereas this study places a dedicated encoder for each input. The primary-input encoder E_{main} converts $\bar{z}_{lr}$, and the auxiliary-DTM encoder E_{aux} converts $\bar{z}_{aux}$ and T, into feature maps with three convolution layers each. The two feature maps are concatenated along the channel dimension and compressed to the number of channels of the RCAB model by the single convolution layer of the fusion layer G (mid-fusion). When there are multiple auxiliary DTMs, an encoder can be provided for each of them and their feature maps concatenated.

The fused feature map is passed to the RCAB model B, which corresponds to the body of RCAN. The RCAB model B consists of 20 RCABs in series; each RCAB is a residual block that adds to its input the result of a convolution, a ReLU, a convolution, and channel attention applied in this order. Every ten RCABs are grouped into a residual group with a skip connection, and after the last convolution of B, the input of the whole of B is added (corresponding to the long skip connection of RCAN). We increased the number of RCABs from the ten of Helmy et al. (2026) to 20 to adjust the capacity to the training data, which are more abundant than in the previous study. The output of B is enlarged to the output grid by the progressive upsampling P in three stages of 2.5×, 2×, and 2×. Each stage consists of bilinear interpolation, a convolution, and a LeakyReLU. Finally, the single convolution layer of the output layer aggregates the features into one channel, which is the output of f; adding the Global skip $U(\bar{z}_{lr})$ to it gives the prediction in normalized space $\hat{Y}$ of Eq. (4.1).

4.1.4 Loss function

As the loss function, we use the mean of the elevation loss L_{elev} and the slope loss L_{slope}, the combination that Helmy et al. (2026) found best. For the training target Y and the prediction $\hat{Y}$, let M be the set of valid pixels, and let M_x and M_y be the sets of positions at which both of the two adjacent pixels needed for the forward differences $(\nabla_x X)_{i,j} = X_{i,j+1} - X_{i,j}$ and $(\nabla_y X)_{i,j} = X_{i+1,j} - X_{i,j}$, respectively, are valid. The losses are defined as follows.

$$L_{elev} = \frac{1}{|M|} \sum_{(i,j)\in M} \left| \hat{Y}_{i,j} - Y_{i,j} \right| \tag{4.3}$$

$$\begin{aligned} L_{slope} = {} & \frac{1}{|M_x|} \sum_{(i,j)\in M_x} \left| (\nabla_x \hat{Y})_{i,j} - (\nabla_x Y)_{i,j} \right| \\ & + \frac{1}{|M_y|} \sum_{(i,j)\in M_y} \left| (\nabla_y \hat{Y})_{i,j} - (\nabla_y Y)_{i,j} \right| \end{aligned} \tag{4.4}$$

$$Loss = (L_{elev} + L_{slope})/2 \tag{4.5}$$

For Y and $\hat{Y}$, we use the values normalized to the deviation from the base elevation described in Section 4.1.1. Because the prediction and the training target are normalized with the same base elevation, each of the losses in Eqs. (4.3) and (4.4) in normalized space is $1/k$ times the value of the same expression evaluated with elevations in meters. Real DTMs contain missing values. The loss and the evaluation metrics are therefore computed only on the set of valid pixels M described above (M_x and M_y for the gradients).

4.2 Geolocation correction

In geolocation correction, the position of a footprint is moved horizontally, the elevation at each position is read from a high-resolution DTM, and it is compared with the ground elevation observed by GEDI. In this study, the DTM used for this comparison is called the reference DTM or the reference surface. The reference DTMs used in this study include the high-resolution DTM, the 1 m resolution DTMs generated by super-resolution, and the 10 m resolution DTM interpolated bilinearly. All reference DTMs are 1 m resolution raster data, and each pixel has one elevation value representing the area that it covers and the coordinates of the center of that area. The correction searches for the position at which the elevation of the reference DTM best matches the observed elevation and moves the footprint there (Tang et al., 2023; Schleich et al., 2023; Li et al., 2025). The horizontal vector by which a footprint is moved is called the offset.

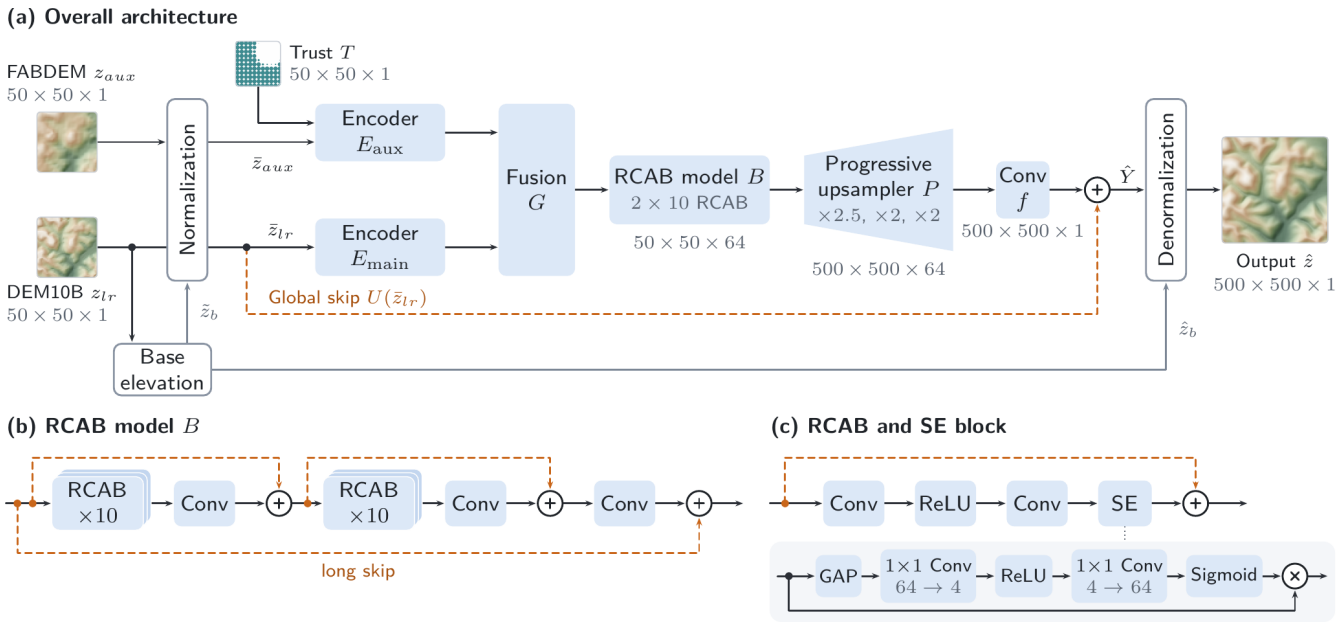


Fig. 4.1: Architecture of the super-resolution model. (a) Overall architecture. (b) RCAB model B. (c) Structure of an RCAB and of channel attention (Squeeze-and-Excitation; SE). GAP denotes global average pooling. The details of each layer are given in Appendix B. The FABDEM image in (a) is adapted from FABDEM V1-2 (Neal and Hawker, 2023), and the output image $\hat{z}$ is derived from it; these two images are licensed under CC BY-NC-SA 4.0.

The unit for which an offset is estimated differs among studies. Tang et al. (2023) estimated, for each orbit, one offset common to all footprints of the same beam. Schleich et al. (2023) estimated an offset for each cluster of about 50 temporally adjacent footprints. Li et al. (2025) distinguished group-level correction, which gives one offset to each combination of orbit and beam, from point-level correction, which gives an individual offset to each footprint, and applied and compared the two in parallel as mutually independent methods. In this paper, we call the former type of correction beam-level and the latter footprint-level, and we perform geolocation correction by executing the two stages in series. The flow of the correction is shown in Fig. 4.2.

In the footprint-level correction of this study, the position after the beam-level correction is the starting point, and the geolocation error remaining after the beam-level correction is searched for each footprint. When the systematic error of a beam is large, a per-footprint search centered on the original coordinates tends to place the true position at or beyond the edge of the search range, which is disadvantageous for the search. Correcting the systematic error of the whole beam first and then searching individually avoids this disadvantage.

This study combines the correction by grid search and the correction by flow accumulation, described below, as follows. First, the beam-level correction is applied by grid search to all footprints, beam by beam. Appendix D shows that using flow accumulation for the beam-level correction hardly changes the corrected positions or the accuracy. Next, the footprint-level correction is performed with the position reached by the beam-level correction (x_1) as the origin. At this stage, both grid search and flow accumulation are applied, and their results are also compared. Finally, as the differences between correction methods, four results are compared: no correction, correction up to the beam level, and correction up to the footprint level with each of the two methods.

4.2.1 Gaussian-weighted elevation of the reference DTM and the candidate set

A GEDI footprint is not a point but a circle about 25 m in diameter, within which the laser energy increases toward the center. In other words, the terrain observed by GEDI is weighted, and this is reflected in the reference surface used for the correction. The Gaussian-weighted elevation $R(x)$ of the reference DTM at position x is defined as the mean of the pixels of the reference DTM weighted by a two-dimensional Gaussian function centered at x (standard deviation $\sigma = 5.5$ m), and the correction is performed on the surface thus obtained. This treatment is the same as in Tang et al. (2023) and Li et al. (2025). The Gaussian-weighted elevation is used at every stage, in the search, for the correction results, and in the evaluation, regardless of the type of reference DTM. Hereafter, when the meaning is clear, the Gaussian-weighted elevation of the reference DTM is also simply called the reference DTM or the reference surface.

The candidates for the corrected position are the coordinates of the pixels of the reference surface contained in a disc of radius r centered on the origin. This study restricts the candidates to discrete points and thereby aligns the resolution of the corrected positions with that of the reference surface. The origin of the correction is the recorded position x_0 at the beam level and the position after the beam-level correction x_1 at the footprint level. In this study, r is 20 m at both stages.

Using a disc as the candidate set differs from previous

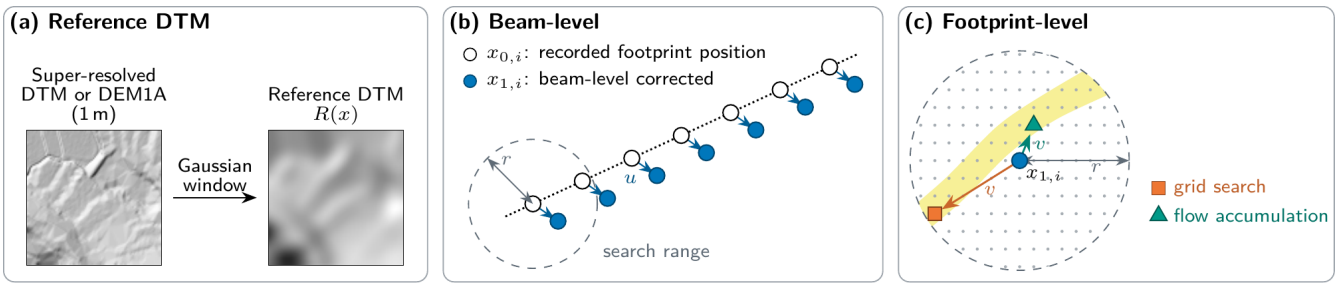


Fig. 4.2: Flow of the geolocation correction. (a) A Gaussian window is applied to the reference DTM to obtain the Gaussian-weighted elevation $R(x)$. (b) Beam-level correction. The dashed circle is the search range of radius r. (c) Footprint-level correction. The yellow band represents the region where candidates with elevations close to the observed elevation line up along a contour line. The square and the triangle are the corrected positions by grid search and by flow accumulation, respectively.

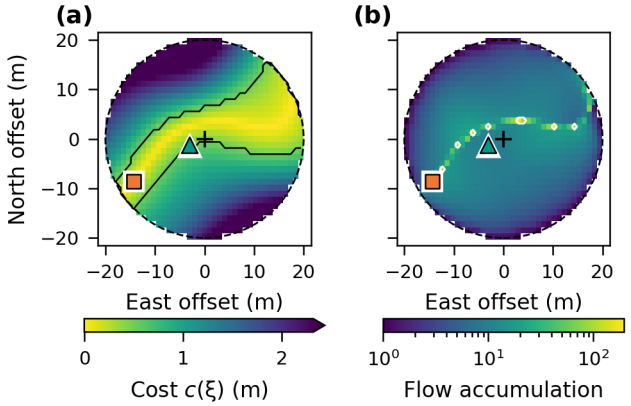


Fig. 4.3: Example of footprint-level correction by grid search and by flow accumulation. The axes are the east–west and north–south distances from the position after the beam-level correction x_1 (+), and the dashed line is the search circle of radius 20 m. (a) Visualization of the cost $c(\xi)$. The black line encloses the candidates whose cost is within 0.5 m of the minimum. (b) Flow accumulation computed from the cost map in (a). The white circles show the cells in the top 1% of flow accumulation. The square is the corrected position by grid search and the triangle that by flow accumulation; they are about 13 m apart.

studies. Tang et al. (2023) searched a 70 m square grid whose axes are the along-track direction of the orbit and the direction perpendicular to it (cross-track). This was based on the assumption that systematic errors originating from attitude and pointing appear along the coordinate system of the orbit. However, the same paper reported that, in the Release 2 data, there was no systematic bias in either the along-track or the cross-track direction and that the offsets were roughly 10 m in magnitude. Li et al. (2025) searched a 30 m square (±15 m) with east–west and north–south axes in 1 m steps, and Schleich et al. (2023) also searched a ±50 m square with east–west and north–south axes in 2 m steps. The point-level offsets reported by Li et al. (2025) showed no discernible tendency in their distribution by direction, and there is no reason to favor a particular direction for footprint-level errors. This study adopted a disc, which does not depend on direction, as the candidate set. This study also identifies correction failures by the Euclidean distance of the displacement, that is, by a circle.

4.2.2 Correction by grid search

Geolocation correction by grid search computes, for each candidate in the candidate set, a cost that represents the degree of agreement with the observed elevation, selects the candidate with the minimum cost, and takes the vector from the origin to that candidate as the offset. Except for the choice of the candidate set and the classification of correction failures described later, this procedure is exactly the same as the group-level correction (corresponding to beam-level) and the point-level correction (corresponding to footprint-level) of Li et al. (2025). With ξ the offset from the origin to a candidate, the cost of one footprint is the absolute difference between the Gaussian-weighted elevation of the reference surface at the candidate position and the observed elevation z_{obs}. In the beam-level correction, the origin is the recorded position x_0, and the cost is

$$c(\xi) = |R(x_0 + \xi) - z_{obs}| \tag{4.6}$$

At the beam level, the cost is the mean of the costs $c_i(\xi)$ of the footprints i belonging to the beam, and the ξ that minimizes it is taken as the offset.

$$\bar{c}(\xi) = \frac{1}{n} \sum_{i=1}^{n} c_i(\xi) \tag{4.7}$$

In the beam-level correction, the ξ that minimizes $\bar{c}(\xi)$ is found with the recorded position x_0 as the origin and is given to all footprints of the beam as the common offset u of the beam. The position after the beam-level correction is $x_1 = x_0 + u$. When grid search is used in the footprint-level correction, the ξ that minimizes $c(\xi) = |R(x_1 + \xi) - z_{obs}|$ is found with x_1 as the origin and taken as the offset v of that footprint, and the position after the footprint-level correction is $x_2 = x_1 + v$. In either case, the corrected position is the coordinates of the selected candidate pixel.

4.2.3 Correction by flow accumulation

The cost map of a single footprint has multiple candidates with costs close to the minimum, and they can appear

at places far apart from each other. In grid search, which selects only the single minimum, which of these candidates is selected switches with a slight error (Fig. 4.3(a)). This study also adopts flow accumulation as a more robust method and always compares it with the results of grid search.

Flow accumulation is a way of selecting the corrected position based on the flow accumulation of hydrological analysis, introduced into GEDI geolocation correction by Schleich et al. (2023). The cost map $c(\xi)$ is regarded as terrain, the same amount of water is placed on every cell, and the water is routed toward lower cost (elevation) with the FD8 algorithm (multiple-direction flow to the eight neighbors). Flow collects in regions of low cost, and a region whose cost is consistently low, including its surroundings, receives more flow than a minimum that is a single deep pit. The flow-weighted centroid of the cells in the top 1% of flow is computed, and the candidate pixel containing the centroid is taken as the corrected position (Fig. 4.3(b)). The fraction of the top 1% is the same as in Schleich et al. (2023).

The flow accumulation of this study differs from that of Schleich et al. (2023) in two respects. First, that paper applied flow accumulation to an error map averaged over a cluster of about 50 temporally adjacent footprints, whereas this study applies it to the cost map of a single footprint after the beam-level correction. Second, that paper used the continuous value of the centroid directly as the corrected position, whereas this study uses the center of the pixel containing the centroid and thereby aligns the resolution of the positions with the candidate set.

4.2.4 Identification of correction failures

In geolocation correction, the wider the search range, the higher the accuracy measured by the agreement between the reference surface and the observed elevation, because more candidates make it easier to find a location whose value is close to the observed elevation. However, this agreement does not guarantee that the correction is correct. Where the terrain has no characteristic relief, or where the reference DTM or the observed elevation is erroneous, the position of minimum cost can be unrelated to the true position. The solutions obtained within the search range therefore include solutions that have small elevation differences but are not corrected to the true position. Although it is difficult to verify directly whether the correction of an individual footprint was correct, the correction result gives clues to its quality. For example, the larger the displacement, the stronger the suspicion that the cost minimization was drawn by an error in the reference DTM or in the observed elevation rather than by the true position, and the lower the quality is assumed to be. In particular, for a footprint whose solution reached the boundary of the candidate set, the reference DTM or the observed elevation may deviate greatly from the true value. We therefore exclude part of the footprints of doubtful quality as correction failures to maintain the quality of the correction results. Previous studies made similar exclusions. Tang et al. (2023) excluded footprints whose elevation difference from the reference DTM exceeded 15 m as outliers, and Li et al. (2025) regarded the cases in which the boundary of the search range was optimal as failures.

The criterion of how much movement is accepted as a successful correction is determined by the balance between the usefulness and the accuracy of the correction results. A stricter criterion increases the accuracy of the remaining footprints but reduces the number of usable footprints. As a simple approach, this study adopts the rule of excluding footprints whose solution reached the boundary of the search circle at any stage of the corrections and evaluating only the remaining footprints. At the beam level, the unit of exclusion is the beam, so multiple footprints are excluded at once. Because a beam that spans test blocks is treated as separate beams, some footprints of the same beam may be excluded while others are not. Footprints without an offset, because the reference DTM required for the search is not available or there is no valid solution in the disc, are also excluded from the evaluation.

4.2.5 Evaluation

Geolocation correction is evaluated from two viewpoints, ground elevation and canopy height. The specific metrics are described in the Results section.

The evaluation by ground elevation uses the difference between the Gaussian-weighted elevation of the high-resolution DTM at the corrected position (defined in the same way as the Gaussian-weighted elevation of the reference DTM) and the ground elevation of GEDI. However, this difference has limitations as an indicator of positional correctness. In particular, when the reference DTM used for the correction is the high-resolution DTM used for the evaluation itself, the elevation difference evaluated after the correction is nothing but the quantity that the correction directly minimized. Li et al. (2025) reported that, when point-level correction was performed with a 1 m resolution DTM, the ground elevation error became almost zero, with an MAE of 0.08 m and a bias of 0.07 m, and referred to this as “overfitting”. A small elevation difference after the correction is certainly desirable, but a small value does not mean that the footprint moved to its true position. An independent evaluation by canopy height is therefore also needed.

In the evaluation by canopy height, RH98 measured at each GEDI footprint is compared with the height of the tree tops detected from the DCHM. RH98 is used rather than RH100, which corresponds to the very top, because it has fewer outliers than RH100 and better represents the canopy height within the footprint (Hofton et al., 2000; Li et al., 2025). The tree-top extraction and the evaluation procedure follow Li et al. (2025): the height of the tallest tree top within a radius of 12.5 m from the corrected position is the value compared. The tree-top detection procedure is described in Appendix A. If the horizontal position has an error, the footprint is placed over a crown different from the actual one, so a reduction in the canopy height difference reflects positional correctness to some extent. Canopy height

can also have errors due to differences in acquisition time and measurement errors, but it is data not used in the correction process, and it is used for comparisons between reference DTMs and between correction methods.

As stated at the beginning of Section 4.2, this study compares four results in total: no correction, correction up to the beam level, and the two footprint-level methods. Because of the failure classification, only footprints whose solution did not reach the boundary in any of the corrections are evaluated. In the evaluation by elevation, the evaluated footprints are nearly the same for all correction methods, so the results can be compared intuitively; however, when the reference DTMs differ, the evaluated footprints and their numbers differ, so a simple comparison is not possible. Furthermore, in the evaluation by canopy height, only footprints for which a tree top was obtained can be validated, so the numbers of evaluated footprints do not match exactly either.

4.3 Super-resolution accuracy sufficient for geolocation correction

A reference surface generated by super-resolution has errors that differ from location to location. In this subsection, the high-resolution DTM (DEM1A) is regarded as the true terrain, and the reference-surface error is defined. How the reference-surface error affects the correction is examined separately for the beam level and the footprint level.

4.3.1 Reference-surface error and the scale seen by the correction

The **reference-surface error** $e(x)$ at position x is defined as the difference between the Gaussian-weighted elevation $R(x)$ of the reference surface and the Gaussian-weighted elevation $R_{DEM1A}(x)$ of the high-resolution DTM.

$$e(x) = R(x) - R_{DEM1A}(x) \tag{4.8}$$

We use $e(x)$, weighted by the Gaussian window, as the error of super-resolution instead of the per-pixel error of the reference DTM in order to discuss the error within the framework of geolocation correction. In the weighted $e(x)$, errors at scales sufficiently smaller than the window width, such as those due to small relief at a scale of a few meters, may cancel out. In other words, the per-pixel error of super-resolution consists of errors that appear in $e(x)$ and errors that exist in terms of super-resolution accuracy but are weakened by the averaging over the Gaussian window and have little influence on the matching cost.

A reference-surface error changes the matching cost and can change the corrected position. With the origin x_0, substituting $R(x) = R_{DEM1A}(x)+e(x)$ into Eq. (4.6) gives

$$\begin{aligned} c(\xi) &= |R_{DEM1A}(x_0+\xi) + e(x_0+\xi) - z_{obs}| \\ &= \left|R_{DEM1A}(x_0+\xi) - \left(z_{obs} - e(x_0+\xi)\right)\right| \end{aligned} \tag{4.9}$$

That is, the reference-surface error enters the cost by changing the target elevation of the comparison at each candidate by $e(x_0+\xi)$, and the size of this change differs from candidate to candidate. The correction cannot detect this change as a reference-surface error, and the corrected position moves along the slope to a location where the elevation on the high-resolution DTM differs by that amount. On this basis, the effects of the reference-surface error on the beam-level and footprint-level corrected positions are examined in turn below.

4.3.2 Effect on the beam-level correction

In the beam-level correction as well, the cost per footprint is $c_i(\xi) = |R_{DEM1A}(x_{0,i}+\xi) - z_{obs,i} + e(x_{0,i}+\xi)|$, as in Eq. (4.9), and the set of candidates that minimize the cost of footprint i is the contour line on which the elevation of the high-resolution DTM equals $z_{obs,i} - e(x_{0,i}+\xi)$. That is, the reference-surface error moves this contour line along the slope away from the contour line on which the elevation equals $z_{obs,i}$.

However, it is difficult to estimate from this relationship how much the reference-surface error moves the offset of an individual beam. First, the reference-surface errors are not independent between footprints but have a spatial structure. Second, the terrain has a complex structure within the search circle, and the reference-surface error is not uniform within the search circle either. Quantifying the effect on the offset while taking these structures into account is beyond the scope of this study.

Nevertheless, the beam-level corrected position is not somewhere on the n contour lines but the minimum of the mean cost $\bar{c}(\xi)$ in Eq. (4.7). Because the beam-level correction determines one offset by matching the sequence of the observed elevations of many footprints against the terrain of the reference surface at once, we consider that the effects of the errors that differ between footprints cancel out among the many footprints and that the offset is hardly dragged by large errors of a few footprints. If this cancellation works, its effect should be stronger for a larger number of footprints n in the beam, and the difference in the offset should decrease with n even for a similar reference-surface error.

In Section 5.4.1, whether the reference-surface error changes the beam-level corrected position is examined directly by whether the beam-level offset u estimated with the super-resolved reference DTM agrees with that estimated with the high-resolution DTM. The degree of agreement is also shown by the number of footprints n in the beam. The mean absolute value and the standard deviation of the per-footprint $e(x_{1,i})$ are shown as the magnitude of the error before cancellation.

4.3.3 Identity for the footprint-level correction

Because the footprint-level correction by grid search selects the candidate that minimizes the cost $|z_{obs} - R(x_1+\xi)|$, the residual after the correction is zero if there is a candidate that matches the observed elevation. When the reference surface needs to be speci-

fied, it is added to the position symbol as a superscript: the position corrected at the footprint level with the super-resolved reference surface R_{M1} is written x_2^{M1}, and, for comparison, the position corrected with the high-resolution DTM R_{DEM1A} is written x_2^{DEM1A}. When the residual is zero in both corrections, the following holds.

$$z_{obs} = R_{DEM1A}(x_2^{DEM1A}) = R_{M1}(x_2^{M1}) \tag{4.10}$$

Substituting $R_{M1}(x_2^{M1}) = R_{DEM1A}(x_2^{M1}) + e(x_2^{M1})$ into Eq. (4.10), the elevation difference between the two corrected positions on the high-resolution DTM becomes

$$R_{DEM1A}(x_2^{DEM1A}) - R_{DEM1A}(x_2^{M1}) = e(x_2^{M1}) \tag{4.11}$$

That is, compared with the corrected position from the high-resolution DTM, the corrected position from the super-resolved reference surface lies at a location whose elevation on the high-resolution DTM differs by $e(x_2^{M1})$. When the residuals are not zero, the difference between the two residuals $z_{obs} - R_{M1}(x_2^{M1})$ and $z_{obs} - R_{DEM1A}(x_2^{DEM1A})$ is added to the right-hand side, but, as shown in the Results section, the two residuals are smaller than e. From this relationship, $z_{obs} - R_{DEM1A}(x_2^{M1})$, which evaluates the position corrected with the super-resolved reference surface on the high-resolution DTM, is

$$z_{obs} - R_{DEM1A}(x_2^{M1}) = R_{M1}(x_2^{M1}) - R_{DEM1A}(x_2^{M1}) = e(x_2^{M1}) \tag{4.12}$$

which shows that it measures not the correctness of the correction result but the reference-surface error itself at the corrected position. In the Results section, we confirm that the elevation difference between the two corrected positions agrees with $e(x_2^{M1})$.

5 Results

Using the super-resolution models and the geolocation correction methods described in the Methods section, we corrected the geolocation of GEDI data in western Japan. We first describe the dataset created for training and then the validation results.

5.1 Experimental setup

5.1.1 Dataset

This study targets forested areas of Japan at latitudes of about 30° to 36° and longitudes of about 128° to 135°. The unit of data used for training and evaluation is a patch of 20 × 20 arcseconds in latitude and longitude, which corresponds to 500×500 pixels on the 1 m resolution digital terrain model (DEM1A), 50×50 pixels on the 10 m resolution digital terrain model (DEM10B), and 21×21 pixels on FABDEM.

The test area is defined as ten blocks delimited by coordinates. Each block spans 20 arcminutes in latitude by 30 arcminutes in longitude, corresponding to one quarter of a primary mesh, and was selected by the authors to include areas where forests and mountains extend. Around each test block, a buffer extending 5 arcminutes (about 9 km) in each of the latitude and longitude directions is set, and the area within the buffer is used for neither training nor validation. The area that belongs to neither the test area nor the buffers is split into training and validation areas by random splitting in units of secondary meshes (about 10 km square). The fraction of secondary meshes assigned to validation is 15%.

Table 5.1: Numbers of patches and areas of the training, validation, and test splits. The areas are approximate.

Split	Patches	Ground area (km^2)
train	261,294	25,663
valid	46,164	4,522
test	67,170	10,959
Total	374,628	41,145

The patches used for training and validation are placed inside tertiary-mesh tiles with a stride of 200 pixels, whereas the patches of the test blocks are placed at 400-pixel intervals on an absolute grid so that they cover the whole block without gaps. In both cases, the patch edges are placed on 10 m pixel boundaries at integer arcseconds (details in Appendix C).

Of the extracted patches, those with at least 90% valid DEM1A pixels, 100% valid DEM10B pixels, and at least 95% valid FABDEM pixels were used for training and evaluation. However, patches in which non-natural classes such as urban areas and water bodies occupy 80% or more of the area in the High-Resolution Land Use and Land Cover Map were excluded. This procedure yields 261,294 training patches (about 25,700 km^2), 46,164 validation patches (about 4,500 km^2), and 67,170 test patches in total (10 blocks, about 11,000 km^2 in total) (Fig. 3.2, Table 5.1).

5.1.2 Reference DTMs compared

The 10 m resolution DTM is super-resolved by the super-resolution models and evaluated against the 1 m resolution DTM. Geolocation correction is also performed with the generated reference surfaces, and its results are evaluated. The five reference surfaces compared are generated as follows.

- (M0) A reference surface obtained by bilinear interpolation of DEM10B onto the 1 m resolution grid.
- (M1) A reference surface generated by the super-resolution model of Section 4.1 with DEM10B as the primary input and FABDEM as the auxiliary DTM.
- (M2) A reference surface generated by a model trained in the same way as (M1) but without the FABDEM input. FABDEM is not used in validation or testing either.

- (M3) A model trained in the same way as (M1) but with a synthetic DTM created from DEM1A (ground truth), instead of DEM10B, as input. The input in validation and testing is also synthetic data.

- (M4) A model trained in the same way as (M3) but without the FABDEM input. FABDEM is not used in validation or testing either.

The input data differ among them. In particular, the models without the FABDEM input do not perform mid-fusion and have no encoder for FABDEM. Hereafter, the notation (M0) to (M4) refers not only to the bilinear interpolation or the super-resolution model itself but also to the generated reference surface and to the results of geolocation correction with that reference surface.

5.1.3 Training

We trained the super-resolution models with the training patches. Adam was used for optimization, and MultiStepLR was applied as the learning-rate scheduler. The initial learning rate was 1×10^{-4}, and it was halved at epochs 40, 60, 80, and 90. The batch size was 20, the maximum number of epochs was 100, and early stopping was not used.

During training, one of eight transformations, consisting of rotations by multiples of 90° and flips about the vertical or horizontal axis, was applied at random to each input pair. This was done to reduce the strong directional bias of the mountains in the study area. The model that minimized the RMSE on the validation patches was taken as the best model.

5.1.4 Evaluation metrics

The accuracy of super-resolution is evaluated for elevations in meters on the valid DEM1A pixels of the test patches. The elevation error, that is, the difference obtained by subtracting the DEM1A value from the value of the generated surface, is expressed by the RMSE and the MAE over all pixels of all test patches, the mean of the difference (Avg. Bias), and the standard deviation across patches of the per-patch mean difference (SD Bias). SD Bias represents the size of the elevation deviations that vary from patch to patch. The reproduction of terrain shape is evaluated by the RMSE of the slope angle and of the aspect computed with the Sobel filter (RMSE-Slope, RMSE-Aspect) and by the Pearson correlation coefficient and the Spearman rank correlation coefficient. RMSE-Slope and RMSE-Aspect follow the definitions of Zhang et al. (2022), and the correlation coefficients are computed for each patch and averaged after Fisher's z-transformation. The improvement over bilinear interpolation is expressed by the reduction rate of the RMSE.

Table 5.2 shows the results of super-resolving the 10 m resolution DTM in the test area and comparing it with DEM1A. The results of bilinear interpolation of DEM10B and of the synthetic data are also included as baselines.

Next, reference surfaces of the test area were created with the super-resolution models and bilinear interpolation, geolocation correction was performed with these reference surfaces, and the results were evaluated. The correction targets are 333,903 footprints belonging to 2,129 beams in the 10 test blocks. As explained in the Methods section, the geolocation correction is evaluated only on the footprints in the test area whose solution did not reach the boundary of the search circle in any of the corrections. Correction with DEM1A as the reference DTM was performed in the same framework and is used as the reference for the correction results.

In the evaluation by elevation, the Gaussian-weighted elevation of DEM1A is taken at the corrected position, and its residual from the elevation observed by GEDI is expressed by the MAE, RMSE, Bias, and Pearson correlation coefficient. In the evaluation by canopy height, GEDI RH98 is compared with the height of the tree tops detected from the DCHM, and the comparison is expressed by the MAE, RMSE, Bias, rRMSE, and Pearson correlation coefficient. In both cases, Bias is the mean of the difference obtained by subtracting GEDI from the reference data. Only when two methods are compared on the same set of footprints, the improvement rate of method B over method A is defined by the following equation, where MAE_A and MAE_B are the MAEs of methods A and B computed on that same set of footprints, and the improvement rate is in percent.

$$100 \times \left(1 - \frac{\mathrm{MAE}_B}{\mathrm{MAE}_A}\right) \tag{5.1}$$

The influence of the reference DTM on the correction results is examined by the agreement with the DEM1A-based corrected positions and by the reference-DTM error $e(x)$. The agreement of corrected positions is measured by the magnitude of the difference in the offset u at the beam level and by the distance between the corrected positions x_2 at the footprint level. The error $e(x)$ is evaluated at the position after the beam-level correction x_1 and at the position after the footprint-level correction x_2. Both are computed on the common set of footprints (beams at the beam level) that were evaluated with both the compared reference DTM and DEM1A.

Tables 5.3 and 5.4 show the results, including those with DEM1A as the reference DTM. Table 5.3 shows the results evaluated by elevation, and Table 5.4 those evaluated by canopy height. The evaluation by canopy height is performed only in five of the ten test blocks (5334_SE, 5234_NW, 5033_NE, 5033_SE, and 4932_NE). The numbers of evaluated footprints in Tables 5.3 and 5.4 are those after removing correction failures; in Table 5.3 they correspond to 58.3% ((M0)) to 69.3% (DEM1A) of all correction targets. Most of the removed footprints are those whose solution reached the boundary of the search circle in the footprint-level grid search. Only the beam-level rows of Table 5.3 have one or two fewer evaluated footprints than the other stages, because for some footprints the Gaussian-weighted elevation of DEM1A could not be obtained at the position after the beam-level correction.

Table 5.2: Overall comparison of the super-resolution models. The reference surfaces generated by the super-resolution models and the elevation surfaces created by bilinear interpolation are evaluated on all 67,170 test patches. Because interpolating DEM10B, which is real data, and interpolating the synthetic data give very different results, two results are given for bilinear interpolation.

Model	Input	RMSE (m)	MAE (m)	Avg. Bias (m)	SD Bias (m)	RMSE-Slope (°)	RMSE-Aspect (°)	Pearson r	Spearman ρ
Bilinear	DEM10B	5.74	4.26	1.611	2.673	13.6	60.7	0.927	0.915
M1	**DEM10B + FABDEM**	**3.80**	**2.81**	**0.098**	**1.622**	**11.6**	**53.4**	**0.962**	**0.956**
M2 DEM10B only	DEM10B	5.29	3.91	0.115	2.607	12.5	57.6	0.934	0.924
Bilinear	Synthetic	0.95	0.63	0.005	0.050	9.2	41.0	0.997	0.997
M3 synthetic	Synthetic + FABDEM	0.42	0.27	0.001	0.003	6.6	32.3	0.999	0.999
M4 synthetic only	Synthetic	0.42	0.27	0.000	0.003	6.7	32.3	0.999	0.999

Table 5.3: Evaluation of elevation accuracy. The results of the geolocation correction are evaluated by elevation for the target footprints in the test area.

Reference DTM	Correction stage	Evaluated	MAE (m)	RMSE (m)	Bias (m)	Pearson r
M0	No correction	194,556	5.05	6.76	-1.59	0.9996
	beam-level	194,555	4.35	5.85	-1.59	0.9997
	beam-level+ footprint-level(gs)	194,556	3.92	5.16	-1.79	0.9998
	beam-level+ footprint-level(fa)	194,556	3.84	5.08	-1.72	0.9998
M1	No correction	212,042	4.84	6.46	-0.97	0.9996
	beam-level	212,041	3.91	5.23	-0.87	0.9998
	beam-level+ footprint-level(gs)	212,042	2.57	3.38	-0.24	0.9999
	beam-level+ footprint-level(fa)	212,042	2.61	3.45	-0.29	0.9999
M2	No correction	198,512	4.85	6.48	-1.01	0.9996
	beam-level	198,511	4.12	5.52	-0.95	0.9997
	beam-level+ footprint-level(gs)	198,512	3.55	4.69	-0.42	0.9998
	beam-level+ footprint-level(fa)	198,512	3.45	4.58	-0.46	0.9998
M3	No correction	230,903	4.73	6.30	-0.81	0.9997
	beam-level	230,901	3.72	4.95	-0.74	0.9998
	beam-level+ footprint-level(gs)	230,903	0.09	0.53	-0.04	1.0000
	beam-level+ footprint-level(fa)	230,903	0.96	1.71	-0.10	1.0000
M4	No correction	230,838	4.73	6.30	-0.80	0.9997
	beam-level	230,836	3.72	4.94	-0.73	0.9998
	beam-level+ footprint-level(gs)	230,838	0.09	0.53	-0.04	1.0000
	beam-level+ footprint-level(fa)	230,838	0.96	1.71	-0.10	1.0000
DEM1A	No correction	231,240	4.73	6.30	-0.81	0.9997
	beam-level	231,238	3.72	4.95	-0.73	0.9998
	beam-level+ footprint-level(gs)	231,240	0.05	0.52	-0.04	1.0000
	beam-level+ footprint-level(fa)	231,240	0.95	1.71	-0.10	1.0000

5.2 Super-resolution accuracy

5.2.1 Overall accuracy

According to Table 5.2, the reference surface generated by (M1) reduced the RMSE by 33.9% relative to bilinear interpolation, from 5.74 m to 3.80 m. For (M2), which does not take FABDEM as input, the RMSE remained at 5.29 m, so most of the improvement of (M1) over bilinear interpolation is due to the contribution of the auxiliary DTM. Comparing (M1) and (M2) shows that the standard deviation of the bias in (M1) is about 40% smaller than in bilinear interpolation and (M2). This can be interpreted as follows: the model can learn to remove a systematic error that is constant over the whole area from the primary input of this study (DEM10B) alone, but an auxiliary input whose origin differs from that of the primary input is needed to greatly reduce the elevation deviations that vary from place to place and the errors of individual patches.

For (M3) and (M4), which use synthetic data, the error with respect to the ground-truth data is extremely small, with an RMSE below 1 m even for bilinear interpolation. (M3) and (M4) can halve the RMSE further, which shows the effectiveness of the super-resolution model itself. In both cases, the bias is extremely small, and there is almost no difference in accuracy between (M3) and (M4), which differ only in whether FABDEM is used. We consider that FABDEM does not contribute to the accuracy because no bias arises when the synthetic data are created.

5.2.2 Terrain roughness and accuracy

In super-resolution, the terrain roughness that affects accuracy is the unevenness of the terrain that does not appear in the input DTM of 10 m resolution. The super-resolution model adopted in this study uses the Global skip, and what the model learns is the residual obtained by removing the smoothed surface of bilinear interpola-

Table 5.4: Evaluation of canopy height accuracy.

Reference DTM	Correction stage	Evaluated	MAE (m)	RMSE (m)	Bias (m)	Pearson r
M0	No correction	57,544	5.49	7.55	-0.90	0.502
	beam-level	57,554	5.41	7.46	-0.90	0.516
	beam-level+ footprint-level(gs)	57,539	5.37	7.46	-0.95	0.519
	beam-level+ footprint-level(fa)	57,563	5.30	7.38	-0.98	0.532
M1	No correction	62,315	5.46	7.53	-1.32	0.501
	beam-level	62,324	5.36	7.40	-1.32	0.520
	beam-level+ footprint-level(gs)	62,308	5.31	7.41	-1.51	0.527
	beam-level+ footprint-level(fa)	62,306	5.24	7.34	-1.51	0.539
M2	No correction	58,179	5.43	7.47	-1.38	0.518
	beam-level	58,183	5.34	7.37	-1.38	0.533
	beam-level+ footprint-level(gs)	58,178	5.31	7.38	-1.56	0.538
	beam-level+ footprint-level(fa)	58,199	5.23	7.31	-1.56	0.550
M3	No correction	66,211	5.38	7.44	-1.38	0.539
	beam-level	66,215	5.27	7.30	-1.39	0.559
	beam-level+ footprint-level(gs)	66,204	5.09	7.18	-1.61	0.582
	beam-level+ footprint-level(fa)	66,223	5.02	7.13	-1.62	0.591
M4	No correction	66,263	5.38	7.41	-1.39	0.541
	beam-level	66,266	5.26	7.27	-1.39	0.561
	beam-level+ footprint-level(gs)	66,251	5.09	7.15	-1.60	0.583
	beam-level+ footprint-level(fa)	66,280	5.02	7.09	-1.62	0.593
DEM1A	No correction	66,322	5.38	7.42	-1.37	0.540
	beam-level	66,333	5.26	7.28	-1.38	0.560
	beam-level+ footprint-level(gs)	66,313	5.09	7.18	-1.59	0.580
	beam-level+ footprint-level(fa)	66,339	5.02	7.11	-1.61	0.591

tion from the terrain. The more complex this residual is, the more difficult super-resolution becomes. In this study, the amount of sub-grid terrain variation was quantified by $\mathrm{SD}_{\mathrm{restopo}}$ defined in Eq. (3.2). We computed $\mathrm{SD}_{\mathrm{restopo}}$ of the reference surfaces for all test patches and created density distributions of the values. Fig. 5.1 shows the density distributions for the reference surfaces generated by (M1) and (M3), the reference surfaces created by bilinear interpolation, and DEM1A. All the density distributions are unimodal and, by the definition of the index, capture the fine-scale character of each reference surface. Fig. 5.2 shows examples of super-resolution by (M1). The output of (M1) roughly matches DEM1A in the arrangement of valleys and ridges but does not reproduce the fine relief seen in DEM1A. The per-pixel residual from the smoothed surface, $|r_i - \mu_r|$, is also visualized (Fig. 5.3). The unevenness increases in the order of the (M1) reference surface, bilinear interpolation, the (M3) reference surface, and DEM1A. In the surface generated by bilinear interpolation of DEM10B, the seams between the 10 m resolution pixels become creases on the generated surface, and residuals appear only on the grid lines. No such structure is seen in the reference surfaces of (M1) and (M3), where the magnitude of the residual changes continuously.

We can consider that the model selection that prioritizes numerical accuracy appears in the distributions of $\mathrm{SD}_{\mathrm{restopo}}$ for (M1) and (M3). The reference surface of (M1) has less fine variation than bilinear interpolation, whereas the distribution of (M3), which was trained and evaluated with synthetic inputs, lies between bilinear interpolation and DEM1A, and (M3) builds finer terrain details than (M1). We consider that the distribution of (M1) lies to the left of that of bilinear interpolation because DEM10B lacks fine structure and because the model generates only the terrain that can be predicted from the input and takes a smooth shape where it cannot predict. Because (M3) receives more information as input, it builds finer terrain details than (M1) or bilinear interpolation. The amount of generated detail thus changes with the input information, which is consistent with a conservative reconstruction of the terrain. However, this analysis alone cannot show that no spurious terrain is generated.

The change in super-resolution accuracy with $\mathrm{SD}_{\mathrm{restopo}}$ is visualized in Fig. 5.4. In the range of $\mathrm{SD}_{\mathrm{restopo}}$ from 0.2 to 0.8, to which most DEM1A patches belong, the accuracy of super-resolution by (M1) improved by 31% to 36% compared with bilinear interpolation, so we consider that the change in accuracy due to terrain roughness is small in the range where most of the data lie.

5.3 Accuracy of geolocation correction

In the evaluation by elevation in Table 5.3, the ground elevation MAE of (M1) decreased from 4.84 m without correction to 3.91 m after the beam-level correction and to 2.57 m (grid search) and 2.61 m (flow accumulation) after the footprint-level correction. With DEM1A as the reference DTM, it changes from 4.73 m to 3.72 m (beam-level), 0.05 m (grid search), and 0.95 m (flow accumulation). The beam-level improvement rates obtained

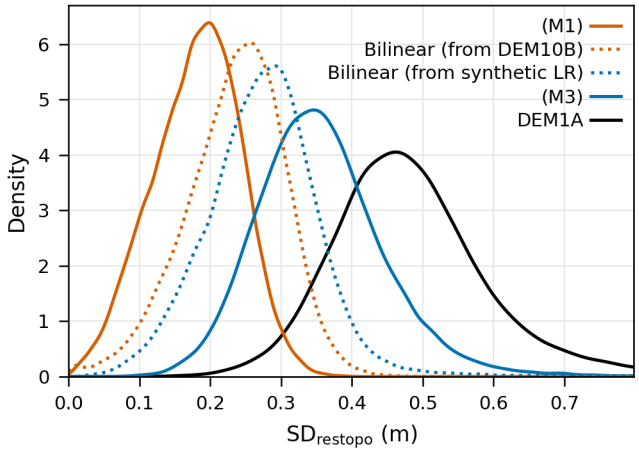


Fig. 5.1: Density distributions of $SD_{restopo}$ of the reference surfaces generated over the test area. For bilinear interpolation, two results are shown: the interpolation of DEM10B and the interpolation of the synthetic data.

with Eq. (5.1) are similar, 19% for (M1) and 21% for DEM1A. The residual of about 2.6 m that remains for (M1) after the footprint-level correction has the same magnitude as the error of the super-resolution model itself (MAE of 2.81 m in Table 5.2). As shown by Eq. (4.12), when the reference DTM is (M1), the residual measured against DEM1A at the corrected position is nothing but the reference-DTM error $e(x_2^{M1})$ at that position. That this relationship also holds footprint by footprint is confirmed in Fig. 5.7. The same applies to (M0) and (M2); for example, the residuals of (M2) after the footprint-level correction, 3.55 m and 3.45 m, are close to its super-resolution MAE of 3.91 m.

In Table 5.4, evaluated by canopy height, the MAE after the footprint-level correction (flow accumulation) is 5.24 m for (M1) and 5.02 m for DEM1A, a difference of 0.22 m. The values of (M2) are smaller than those of (M1) largely because of the difference in the sets of evaluated footprints. On the common set of footprints evaluated for (M1), (M2), and DEM1A (44,630 footprints), the MAEs after the footprint-level correction (flow accumulation) are 4.97 m, 5.01 m, and 4.86 m, respectively. Comparing the correction results of (M3), (M4), and DEM1A, the values were almost the same for both elevation and canopy height (Tables 5.3 and 5.4). The results with DEM1A are consistent with those of Li et al. (2025), but the MAE and RMSE are slightly smaller in this study, possibly because more data with outlying values were excluded than in the previous study.

By correction method, the elevation residuals in Table 5.3 decrease in the order of no correction, beam-level, and footprint-level for every reference DTM. Of the two footprint-level methods, grid search selects a candidate that matches the observed elevation, whereas flow accumulation selects the centroid of the cells in the top 1% of flow accumulation, so the elevation residual with respect to the reference DTM used for the correction is smaller for grid search by construction. Note that the residuals in Table 5.3 are evaluated with DEM1A, so this order does not necessarily hold when the reference DTM is not DEM1A. This order holds for DEM1A (0.05 m and 0.95 m), for (M1) (2.57 m and 2.61 m), and for (M3) and (M4) (the same values as DEM1A). For (M0) and (M2), the values are 3.92 m and 3.84 m and 3.55 m and 3.45 m, respectively, and flow accumulation is smaller. In canopy height (Table 5.4), flow accumulation gave a smaller MAE than grid search for every reference DTM, and, in particular, with (M1) and DEM1A as the reference DTM, this tendency was consistent in all test blocks (Fig. 5.5). The elevation residual is the quantity that grid search directly minimizes, and its size does not represent the order of positional correctness. Flow accumulation is better in canopy height, which is the basis for recommending it for the footprint-level correction. The reason why grid search is inferior is discussed in the Discussion section.

5.4 Reference-DTM error and corrected positions

The differences in accuracy between correction stages evaluated by canopy height are small, and even between reference DTMs, the difference in MAE between (M1) and DEM1A is only 0.22 m (0.11 m on the common set); therefore, whether the reference DTM generated by super-resolution gives the same correction results as DEM1A cannot be judged from the canopy height accuracy alone. In the following, we therefore examine the influence of the reference DTM on the correction results in three ways: the agreement with the DEM1A-based corrected positions (Table 5.5, Fig. 5.6), the verification of Eqs. (4.11) and (4.12) (Fig. 5.7), and the descriptive statistics of the reference-DTM error (Table 5.7).

5.4.1 Agreement with the DEM1A-based corrected positions

Fig. 5.6 shows the distributions of the offsets of the geolocation correction with DEM1A (top row) and the (M1) corrected positions relative to the corresponding DEM1A corrected positions (bottom row). The beam-level offset u spreads over the whole search circle, and its median magnitude is 7.7 m (Table 5.5). The footprint-level offset v spreads almost uniformly over the whole search circle with grid search, whereas it concentrates near the origin with flow accumulation (Fig. 5.6(b)(c)). The discrepancies between the DEM1A and (M1) corrections in the bottom row show that, at the beam level, the discrepancies lie within a narrower range than the distribution of the offset u, whereas, at the footprint level, the discrepancies of the corrected positions spread over a range larger than the search circle.

Table 5.5 shows how far the corrected positions with each of the reference DTMs (M0) to (M3) lie from the DEM1A-based corrected positions. At the beam level, the offset of (M1) was identical to that of DEM1A for 4.3% of the beams, the median magnitude of the difference was 2.4 m, and the difference was within 5 m for 84.9% of the beams (Fig. 5.6(d)). This median difference is about one third of the median magnitude of the DEM1A offset (7.7 m), and, without correction, only

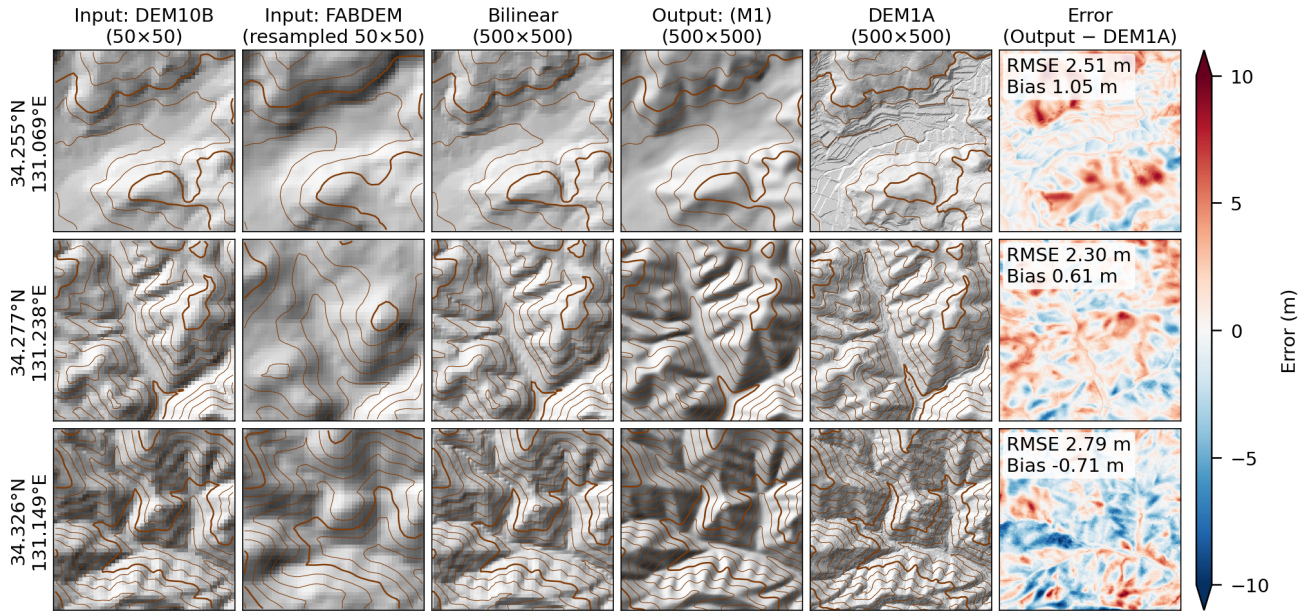


Fig. 5.2: Examples of super-resolution by (M1) for three test patches. From left to right, the columns are the inputs DEM10B and FABDEM, the bilinear interpolation of DEM10B, the output of (M1), DEM1A, and the error obtained by subtracting DEM1A from the output of (M1); the elevation columns are shown as hillshades overlaid with contour lines at 20 m intervals. The three patches are those whose DEM1A $SD_{restopo}$ is at about the 16th, 50th, and 86th percentiles of all test patches, arranged from the top in order from the smoothest terrain. The RMSE and the bias of each patch are shown on its error panel. The FABDEM column is adapted from FABDEM V1-2 (Neal and Hawker, 2023), and the (M1) output and error columns are derived from it; these columns are licensed under CC BY-NC-SA 4.0.

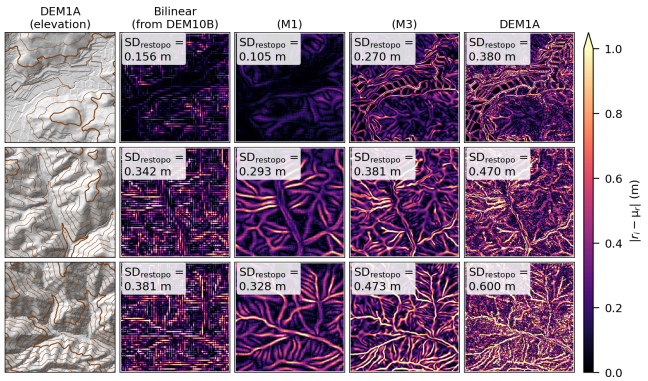


Fig. 5.3: $|r_i - \mu_r|$ of each pixel for the same patches as in Fig. 5.2. The leftmost column shows the hillshade and contour lines of DEM1A as a reference for the terrain. The number at the upper left of each panel is the $SD_{restopo}$ of that panel. The (M1) and (M3) columns are derived from FABDEM V1-2 (Neal and Hawker, 2023) and are licensed under CC BY-NC-SA 4.0.

25% of the beams lie within 5 m of the DEM1A corrected positions. For (M0) and (M2), the medians were both 4.2 m and the fractions within 5 m were 55.7% and 58.8%, respectively, and for (M3), 87.0% were identical. At the footprint level, the median distance between the (M1) and DEM1A corrected positions was 11.6 m for grid search and 5.3 m for flow accumulation (Fig. 5.6(e)(f)), and the distance for flow accumulation is about the same as its median displacement (6.4 m). Even with flow accumulation, the fraction of identical positions was only 1.1% and the fraction within 2.5 m only 16.3% (0.3% and 4.6% for grid search). For (M3), 87.5% of the corrected positions by flow accumulation lie within 2.5 m, which almost reproduces the DEM1A-based corrected positions. With grid search, the solution is indeterminate along the contour line even with DEM1A, so the fraction of identical positions is low, 20.8%, even for (M3). The differences between the (M1) and DEM1A corrected positions have no systematic directional bias, and the medians of the east–west and north–south components are 0 at every stage (Fig. 5.6(d)–(f)).

In summary, the beam-level correction results of (M1) and (M3) almost agree with those of DEM1A, and the degree of agreement decreases for (M0) and (M2), whose reference-DTM errors are larger. The footprint-level correction results agree for (M3), whose reference-DTM error is small, but not for (M0), (M1), and (M2). The degree of agreement follows the order of the magnitude of the reference-DTM error (Table 5.7).

The degree of beam-level agreement increases with the number of evaluated footprints n in the beam (Table 5.6). The median difference in the offset of (M1) is 4.8 m for beams with n below 30, 2.7 m for n from 30 to below 80, 2.1 m for n from 80 to below 150, and 1.6 m for n of 150 or more, and the fraction within 5 m rises from 53.8% to 99.6%. Of the beams whose difference exceeds 5 m, 72% are beams with n below 30. The same tendency holds for (M0) and (M2), and for (M3), whose reference-DTM error is small, the difference is 0 regardless of n. Beams with larger n have slightly smaller DEM1A offsets, but when the magnitude of the DEM1A offset is divided into below 5 m, 5 m to below 10 m, and 10 m or more, the

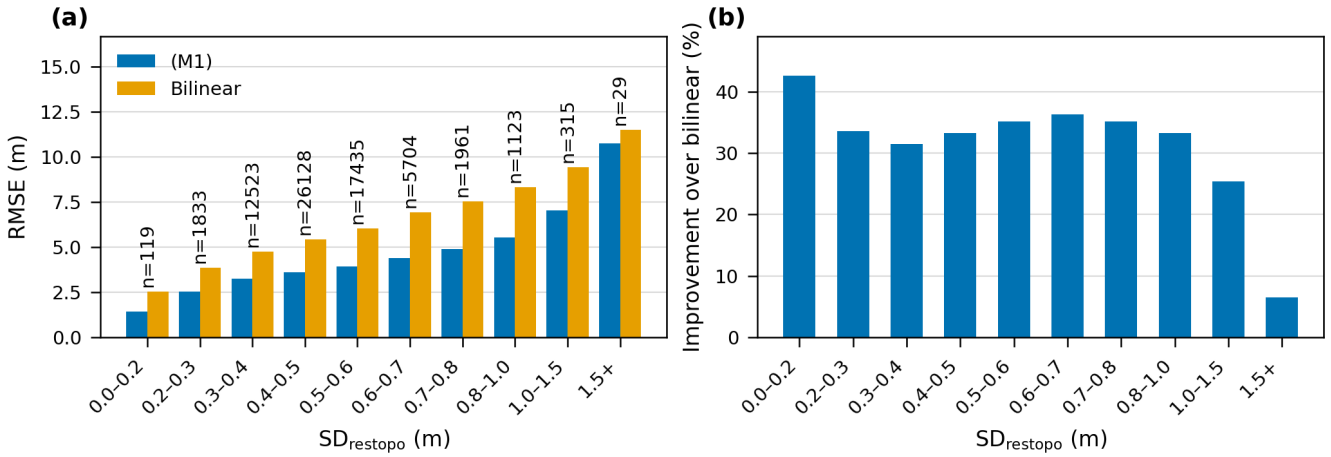


Fig. 5.4: Super-resolution accuracy by class when all test patches are classified by the $SD_{restopo}$ of DEM1A. (a) RMSE of (M1) and of the bilinear interpolation of DEM10B. The numbers above the bars are the numbers of patches in each class. (b) Improvement rate of the RMSE of (M1) over bilinear interpolation. The RMSE was computed from all pixels of the patches in each class.

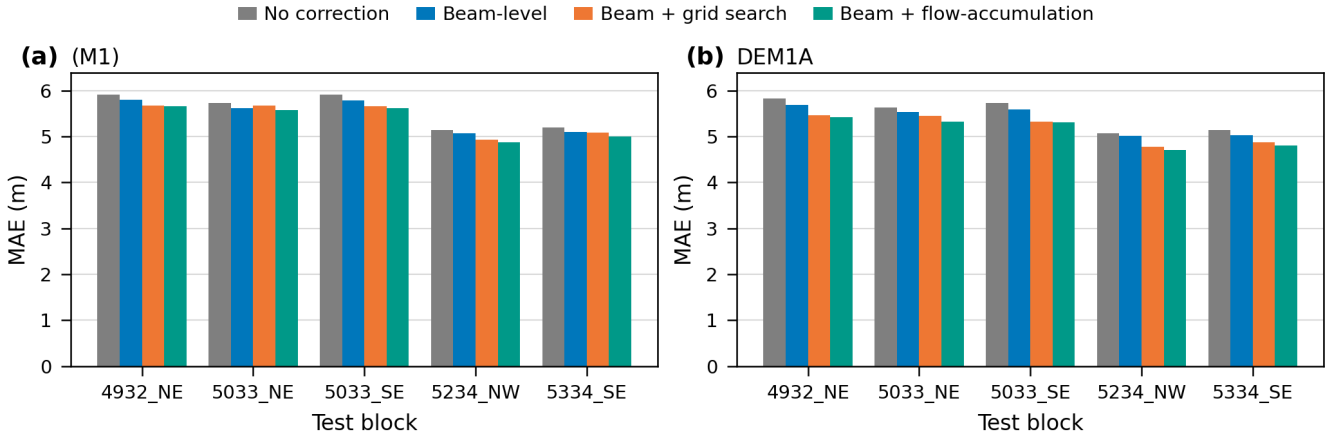


Fig. 5.5: MAE of canopy height in each of the five test blocks where the DCHM is available, for (a) (M1) and (b) DEM1A.

median difference in every class is 4–5 m for beams with n below 30 and 1.6 m for beams with n of 150 or more.

5.4.2 Verification of the identity

Fig. 5.7 shows scatter plots that verify that Eqs. (4.11) and (4.12) hold for the footprint-level correction with (M1). The horizontal axis is the reference-DTM error at the corrected position, $e(x_2^{M1})$, and the vertical axes are the elevation residual measured with DEM1A, $z_{obs} - R_{DEM1A}(x_2^{M1})$, and the elevation difference between the two corrected positions, $R_{DEM1A}(x_2^{DEM1A}) - R_{DEM1A}(x_2^{M1})$. Fig. 5.7(a)(c) show that, for grid search, $z_{obs} - R_{DEM1A}(x_2^{M1}) \approx e(x_2^{M1})$ and $R_{DEM1A}(x_2^{DEM1A}) - R_{DEM1A}(x_2^{M1}) \approx e(x_2^{M1})$ almost hold. That is, at the position after the footprint-level correction with (M1), the elevation residual measured with DEM1A is the reference-DTM error itself, and the (M1) corrected position lies at a location whose elevation differs from that of the DEM1A corrected position by the reference-DTM error. As described in the Methods section, this agreement is a relationship that holds naturally as a consequence of correction by grid search and does not measure the quality of the reference DTM. The points off the diagonal are about 0.7% of the total, and most of them are footprints for which no candidate of the reference DTM within the search circle matched the observed elevation. Flow accumulation selects the centroid of the flow accumulation rather than a candidate that matches the observed elevation, so the points scatter correspondingly (Fig. 5.7(b)(d)).

5.4.3 Reference-DTM error

Table 5.7 shows the descriptive statistics of the reference-DTM error $e(x_1)$ evaluated at the position after the beam-level correction x_1. As defined in Eq. (4.8), $e(x)$ is the difference in Gaussian-weighted elevation between the reference DTM and DEM1A; it evaluates the same elevation difference as the super-resolution accuracy in Table 5.2, but only at the footprint positions instead of at all pixels of the test area, and for values weighted by the Gaussian window instead of pixel values. Because the correction sees the reference DTM only through the Gaussian-weighted elevation $R(x)$, $e(x_1)$ represents the magnitude of the reference-DTM error to which the

Table 5.5: Agreement with the DEM1A-based corrected positions. For the per-beam difference in the offset at the beam level and the distance between the corrected positions at the footprint level, the fraction of exact agreement (the same offset at the beam level and the same pixel at the footprint level), the fractions within 2.5 m and within 5 m, the median, and the number of units are shown. The median displacement of each stage is also given for the reference DTM and for DEM1A.

Reference DTM	Stage	Units	Identical (%)	Within 2.5 m (%)	Within 5 m (%)	Median (m)	Median displacement (m), reference DTM / DEM1A
M0	beam-level	1,701	2.1	23.1	55.7	4.2	8.5 / 7.7
	grid search	165,835	0.2	3.0	10.2	13.4	12.7 / 11.7
	flow accumulation	165,835	0.5	8.5	26.8	7.5	7.2 / 5.4
M1	beam-level	1,743	4.3	55.1	84.9	2.4	8.1 / 7.7
	grid search	185,150	0.3	4.6	14.5	11.6	12.3 / 11.7
	flow accumulation	185,150	1.1	16.3	44.6	5.3	6.4 / 5.5
M2	beam-level	1,689	2.0	24.4	58.8	4.2	8.5 / 7.7
	grid search	171,617	0.2	3.3	10.9	12.8	12.6 / 11.6
	flow accumulation	171,617	0.6	9.8	29.9	7.2	6.9 / 5.3
M3	beam-level	1,822	87.0	99.1	99.8	0.0	8.0 / 8.0
	grid search	212,175	20.8	30.0	40.3	7.2	11.9 / 11.9
	flow accumulation	212,175	34.7	87.5	97.8	1.0	5.8 / 5.8

Table 5.6: Difference in the beam-level offset between (M1) and DEM1A by class of the number of footprints n in a beam. For the same set of beams as in Table 5.5, the number of beams, the median magnitude of the DEM1A offset, the median difference in the offset, and the fraction of differences within 5 m are shown.

Class of n	Beams	Median magnitude of the DEM1A offset (m)	Median difference in the offset (m)	Within 5 m (%)
Below 30	409	8.9	4.8	53.8
30 to below 80	456	8.1	2.7	86.0
80 to below 150	415	7.5	2.1	97.8
150 or more	463	6.2	1.6	99.6
All	1,743	7.7	2.4	84.9

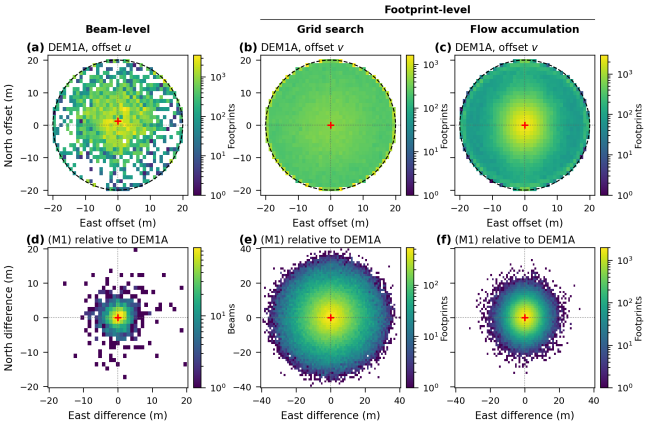


Fig. 5.6: Distributions of the offsets of the geolocation correction. The top row (a)–(c) shows the offsets of the correction with DEM1A: (a) the beam-level offset u (origin at the recorded position x_0), and the footprint-level offset v by (b) grid search and (c) flow accumulation (origin at the position after the beam-level correction x_1). The bottom row (d)–(f) shows the (M1) corrected positions relative to the corresponding DEM1A corrected positions, each of which is taken as the origin: (d) beam-level (per beam), and (e) grid search and (f) flow accumulation (per footprint). The dashed lines in the top row show the search circle of radius 20 m. The red + marks the median.

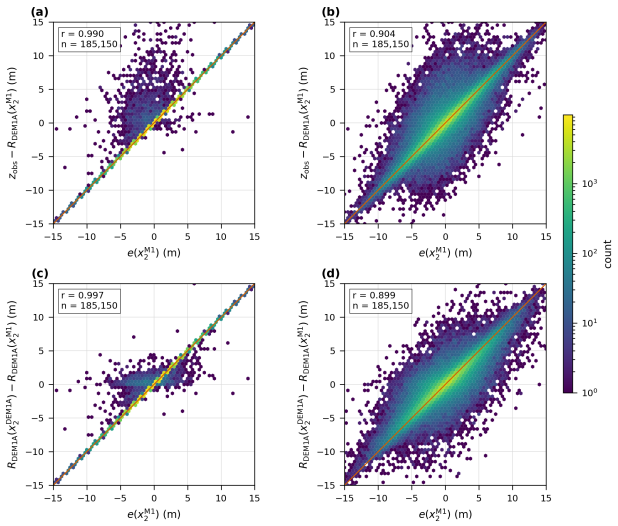


Fig. 5.7: Hexbin scatter plots that verify the relationships of Eqs. (4.11) and (4.12) for the footprint-level correction with (M1). The horizontal axis is the reference-DTM error at the corrected position, $e(x_2^{M1})$. The vertical axis is the elevation residual measured with DEM1A, $z_{obs} - R_{DEM1A}(x_2^{M1})$, in the top row and the elevation difference between the two corrected positions, $R_{DEM1A}(x_2^{DEM1A}) - R_{DEM1A}(x_2^{M1})$, in the bottom row. The left column is grid search and the right column is flow accumulation. The points above the diagonal in (a) are footprints for which no candidate matching the observed elevation existed within the search circle. The Pearson correlation coefficient r and the number of footprints n are shown in each panel.

correction is subject.

For (M1), the per-footprint $e(x_1)$ has a mean of 0.12 m, a standard deviation of 3.32 m, and a mean absolute value of 2.55 m. This standard deviation is only about 10% smaller than the per-pixel RMSE (3.80 m in Table 5.2), so most of the super-resolution error remains even at the scale of the Gaussian window seen by the correction. Among the reference DTMs, the standard deviation of

$e(x_1)$ is remarkably small for (M3), 0.08 m, and increases in the order of (M1), (M2), and (M0), at 3.32 m, 4.59 m, and 4.74 m. This order is the same as the order in which the degree of agreement with the DEM1A-based corrected positions decreases (Table 5.5). (M0) and (M2) differ almost only in the mean (1.55 m and 0.24 m): the super-resolution with DEM10B alone as input removed the deviation common to the whole area but hardly reduced the errors that vary from place to place. The errors that vary from place to place were reduced by (M1), which adds the auxiliary DTM, and its standard deviation is about 30% smaller than that of (M2). This is the same relationship as that seen in the mean and the standard deviation of the bias in Table 5.2. Based on this result, the Discussion section describes where the errors produced in super-resolution come from.

6 Discussion

The question of this study was whether a reference DTM generated by super-resolution gives the same geolocation correction results as DEM1A, and, if not, why. The Results section shows that the answer differs between the correction stages. In the beam-level correction, (M1) gave almost the same offset as DEM1A, and the degree of agreement increased with the number of footprints in a beam. Because the degree of agreement is lower for (M2), which was super-resolved without the auxiliary DTM, this agreement was obtained by super-resolution with the auxiliary DTM added. In the footprint-level correction, the corrected positions of (M1) did not reproduce those of DEM1A but moved to locations where the elevation on DEM1A differs by the reference-DTM error at the corrected position, that is, to locations upslope or downslope of the DEM1A-based corrected positions. Below, we first discuss, for the beam-level correction, where agreement was obtained, how far the mechanism of the agreement can be explained by the findings in the Results section (Section 6.1). We then discuss why, with the same reference DTM, the footprint-level result differed from the beam-level result, and from this derive the reference-DTM accuracy required for footprint-level geolocation correction and the precautions for performing footprint-level correction with a super-resolved reference DTM (Section 6.2). Next, we discuss the possibility that the effect of geolocation correction hardly appears in canopy height (Section 6.3). We then sort out the causes of the reference-DTM error from the input side (Section 6.4) and discuss the implications for the super-resolution of real data (Section 6.5). Finally, we discuss the significance and limitations of this study (Section 6.6).

6.1 Why beam-level offsets agree

In the beam-level correction, (M1), generated by super-resolution, gave almost the same offset as DEM1A. This agreement is not trivial. This is because the difference between the two offsets is much smaller than the magnitude of the offset itself, even though the reference-DTM error around the footprints is too large to be neglected. As described in the Methods section, it is difficult to estimate directly how much the reference-DTM error moves the offset of an individual beam, and this study can go no further than the hypothesis that the errors at individual footprints cancel each other out so that their influence is suppressed.

The findings in the Results section are all consistent with the cancellation hypothesis. The difference between the offset of (M1) and that of DEM1A is approximately one third of the displacement given by the DEM1A-based correction, and there is no systematic preferred direction in the difference. The difference decreases with the number of footprints in a beam, and for beams with many footprints it approaches the pixel spacing of the reference DTM. Beams with more footprints have slightly smaller DEM1A offsets, but the decrease of the difference with the number of footprints remains when beams with similar DEM1A offset magnitudes are compared. Because the offsets agree regardless of the number of footprints under the synthetic-data condition, where the reference-DTM error is almost absent, the instability of the solution in beams with few footprints alone does not produce the offset difference, which is thought to be caused by the reference-DTM error that remains without being canceled out. The lower degree of agreement for (M0) and (M2), whose errors are larger, can be interpreted in the same way. Therefore, although how much of the error is canceled out in an individual beam cannot be identified, the reference-DTM error is thought to be canceled out among footprints in the beam-level correction, and beams that do not agree are mostly beams with few footprints, where the cancellation does not work.

The number of footprints in a beam is a quantity that is known even without DEM1A. Therefore, when beam-level correction is performed with a super-resolved reference DTM, the number of footprints can serve as an indication of the reliability of the correction result.

6.2 Why footprint-level corrections diverge

On the other hand, the reason why the generated reference DTM did not reproduce the DEM1A-based corrected positions in the footprint-level correction lies in the relation between the magnitude of the elevation difference that the two stages try to resolve and the magnitude of the reference-DTM error. After the beam-level correction, an elevation difference between the observed ground elevation and the reference DTM remains; the footprint-level correction tries to resolve it using each footprint alone. As Eq. (4.11) shows, the reference-DTM error then moves the corrected position to a location whose elevation differs by the amount of that error. Therefore, to obtain the same corrected position as DEM1A, the reference-DTM error must be much smaller than the elevation difference that the footprint-level correction tries to resolve. This is the condition on the reference-DTM accuracy required for footprint-level correction. Looking at this relation with the numbers in the Results section, for (M1) the mean absolute value of the reference-DTM

Table 5.7: Descriptive statistics of the reference-DTM error $e(x_1)$: per-footprint mean, standard deviation, and mean absolute value.

Reference DTM	Beams	Footprints	Mean (m)	Standard deviation (m)	Mean absolute value (m)
M0	1,698	165,834	1.55	4.74	3.81
M1	1,742	185,149	0.12	3.32	2.55
M2	1,687	171,616	0.24	4.59	3.51
M3	1,821	212,173	0.00	0.08	0.05

error is 2.55 m, whereas the elevation residual remaining after the beam-level correction is 3.91 m; the two are comparable. For (M2) they are 3.51 m versus 4.12 m and for (M0) 3.81 m versus 4.35 m, which are even closer, whereas for (M3) they are 0.05 m versus 3.72 m, and the error is negligible compared with the elevation difference to be resolved. The degree to which the footprint-level corrected positions agreed with DEM1A (the fraction within 2.5 m with flow accumulation is 87.5% for (M3), 16.3% for (M1), 9.8% for (M2), and 8.5% for (M0)) follows the order of how small the reference-DTM error is relative to the elevation difference to be resolved, and the closer the error is to the elevation difference, the more the corrected position is dominated by the reference-DTM error.

From the above, footprint-level correction with a reference DTM whose accuracy is comparable to that of (M1) is not a substitute for footprint-level correction with DEM1A. If footprint-level correction is to be performed with a super-resolved reference DTM, the following points require attention. First, because the corrected position deviates from the DEM1A-based corrected position by about as much as the displacement made by the correction, the same corrected positions as those of the DEM1A-based correction cannot be expected at all for individual footprints. Second, flow accumulation should be used as the method. Canopy height, which is not used in the correction, was more accurate with flow accumulation in all test blocks for both (M1) and DEM1A, and the corrected positions with flow accumulation were also closer to the DEM1A-based corrected positions. The inferiority of grid search is not limited to (M1) but appears in the same way in canopy height when DEM1A is used as the reference DTM, so its cause is not the reference-DTM error but the nature of the method. That nature is the instability of the solution described in the Methods section. The cost map of a single footprint has multiple near-minimum candidates lying along a contour line, and the solution of grid search, which selects only one point, switches between them with a slight error. Even under the synthetic-data condition, where the reference-DTM error is almost absent, the corrected position of grid search was in the same pixel as that of DEM1A for only a minority of footprints, whereas flow accumulation almost reproduced the DEM1A-based corrected positions. With a super-resolved reference DTM, the reference-DTM error is added to this instability, so the conservative nature of flow accumulation is all the more important. Third, whether the footprint-level correction makes the position worse than the beam-level corrected position cannot be determined in this study. This study regarded DEM1A as the true terrain and evaluated positions by the agreement with the DEM1A-based corrected positions. The error of DEM1A itself is absorbed into the reference-DTM error, and the DEM1A-based corrected position is not the true position either. Therefore, the agreement of corrected positions in this study measures whether the same result is obtained as with the existing method using DEM1A as the reference DTM, not the closeness to the true position, and for the same reason it cannot measure whether the corrected position from the super-resolved reference DTM moved closer to or farther from the true position. That the true position is unknown is not a limitation specific to this study; directly verifying the correctness of the position requires simulated observations with a known geolocation error (Roy et al., 2021) or validation by independent ground surveys (Tang et al., 2023), which is outside the scope of this study.

6.3 Limitations of the evaluation by canopy height

The reason this study measured the influence of the reference DTM by the agreement with the DEM1A-based corrected positions rather than by canopy height is that the effect of geolocation correction hardly appeared in canopy height. In the evaluation by canopy height, the differences were small both between correction stages and between reference DTMs. Even with DEM1A as the reference DTM, the MAE of canopy height changed only from 5.38 m with no correction to 5.26 m after the beam-level correction and 5.02 m after the footprint-level correction (flow accumulation), and the difference between (M1) and DEM1A is 0.22 m (0.11 m in the common set). For (M3) with synthetic data, the MAE of canopy height agreed with that of DEM1A within 0.01 m, even though approximately 60% of the grid-search corrected positions were more than 5 m away from the DEM1A-based corrected positions. These results suggest that canopy height hardly responds to the displacements of a few meters to somewhat more than ten meters made by geolocation correction. A similar insensitivity has been reported in previous studies (Quiros et al., 2021; Tang et al., 2023; Schleich et al., 2023; Yang et al., 2024). Although direct comparison with most previous studies is not possible because the definitions of canopy height and the target forests differ, when the recorded positions were shifted in eight directions in steps of 5 m up to 20 m, as in Quiros et al. (2021) and Kutchartt et al. (2022), the MAE of canopy height increased only from 5.37 m to at most 5.91 m, whereas the MAE of ground elevation

increased from 5.17 m to at most 9.70 m (Appendix E). Canopy height may be insensitive to positional shifts. However, this is the case in which all footprints are shifted uniformly. When a position is selected for each footprint from the recorded position and the 32 shifted positions, the MAE of canopy height drops to 2.54 m at the positions with the smallest canopy-height error, but the MAE of ground elevation increases to 6.25 m; at the positions with the smallest ground-elevation residual, the MAE of ground elevation drops to 0.41 m, but the MAE of canopy height remains at 5.08 m (Appendix E). In other words, the MAE of canopy height itself can take smaller values, but such values are not of the kind obtained by a correction based on ground elevation and may be smaller than the ideal lower bound reachable by correction. If the lower bound reachable by correction is close to the current accuracy, canopy height is insensitive to correction, but this is difficult to judge with the data of this study.

This property holds regardless of the reference DTM. Hence, "almost the same accuracy in canopy height" does not so much prove that the super-resolved reference DTM gives the same correction results as DEM1A as show that canopy height lacks the discriminating power to distinguish between reference DTMs. What can be clearly stated from canopy height is limited to the direction of accuracy differences that is consistent across all test blocks, such as the ranking of the two footprint-level methods.

Possible causes of the weak effect of correction on canopy height include the tree-top detection method, the fact that on slopes RH98 includes the terrain relief within the footprint and can exceed the tree height (Park et al., 2014; Li et al., 2024), the variation of tree heights within a stand, and the vertical error of GEDI itself; this study has not separated them. The ground elevation and canopy-top elevation of GEDI contain vertical errors that arise when they are identified from the received waveform, and these errors become larger under dense canopies and on steep slopes (Hancock et al., 2019; Liu et al., 2021; Quiros et al., 2021). DTM-based correction cannot distinguish these vertical errors from geolocation errors, and they degrade the accuracy of the correction (Adam et al., 2020; Li et al., 2025). Because these factors are not removed by matching the ground elevation, increasing the agreement of canopy height through correction would require using canopy information in determining the position as well, as in the method that determines the position based on agreement with a canopy-height metric (Wang et al., 2025).

6.4 Sources of the reference-DTM errors

The accuracy required of the super-resolution should be considered not per pixel but at the scale of the window seen by the correction; for example, insufficient reproduction of small-scale relief that is smoothed out by the Gaussian window is not a limiting factor of the correction. In fact, however, the reference-DTM error evaluated per footprint hardly differed from the per-pixel super-resolution error. This means that most of the error of the super-resolution model in this study consists of components at scales that can be represented by a 10 m-resolution DTM, which remain even after averaging with the Gaussian window.

We consider that this error did not arise in the process of super-resolution from 10 m to 1 m resolution, but is the part of the error originally present in the input that could not be removed even by the training and the auxiliary input. The absence of a systematic preferred direction in the difference between the corrected positions indicates that the reference DTM is not horizontally misaligned with DEM1A, but that location-dependent elevation errors move the corrected positions. The primary input, DEM10B, is a DTM produced from the contour lines of topographic maps; it does not contain the shape of the terrain between contour lines, and its elevation accuracy is stated to be within 5 m in standard deviation. For (M2), which used DEM10B alone as input, the standard deviation of the per-patch bias hardly differed from that of bilinear interpolation. What the training could remove was the systematic error common to the whole area, and the location-dependent elevation errors could not be corrected from DEM10B alone. The comparison with synthetic data described below is also consistent with the interpretation that the amount of information in the input is insufficient. Therefore, what is needed to obtain a super-resolution model that is more useful for geolocation correction is not the reproduction of relief on the 1 m grid, but the reduction of the error that the input DTM has at the scale of its own resolution.

The most effective way to reduce the error of the input DTM is to use a higher-quality DTM as input or to add an information source whose origin differs from that of the primary input. For (M1), which added FABDEM, a DTM of a different origin, as the auxiliary input, the standard deviation of the per-patch bias decreased by approximately 40% from (M2), and along with this, the reference-DTM error became smaller, the beam-level agreement increased, and the elevation residual after the footprint-level correction decreased. However, the 30 m-resolution FABDEM cannot represent shapes smaller than several tens of meters, and in forested areas FABDEM itself has errors of several meters (Hawker et al., 2022). Therefore, we consider that, although FABDEM can reduce the bias, it has not sufficiently reduced the error at the scale of the 10 m-resolution DTM.

There are practical constraints on adding input DTMs of different origins. DTMs that measure the same area by a different method at a similar resolution hardly exist, and free DTMs covering the globe are limited to those, like FABDEM, derived by removing vegetation from a 30 m-resolution DSM. On the other hand, optical images are acquired repeatedly over the globe at resolutions of 10 m or finer. In DEM super-resolution, there are studies that restore terrain details using high-resolution aerial photographs or satellite images as auxiliary inputs (Argudo et al., 2018; Kubade et al., 2020; Liu et al., 2026), and in the production of global DTMs, methods that remove vegetation-induced errors of DSMs using vegetation height and cover as predictor variables are

used (Hawker et al., 2022). However, what optical images capture is the surface of the canopy, and super-resolution with images as auxiliary inputs is reported to degrade in densely vegetated areas (Kubade et al., 2020). Although it is difficult to restore terrain details in forested areas directly from optical images, the location-dependent errors of contour-derived DTMs and DSM-derived DTMs are considered to be related to vegetation, so using optical images not as a source of terrain information but as a source of information that explains the error of the input DTM is a direction for future work.

The comparison with synthetic data is also consistent with the interpretation that what limits the capability of the correction is mainly the amount of information in the input. For (M3) and (M4), which used synthetic data produced by coarsening DEM1A as input, the reference-DTM error was far smaller than under the real-data condition, and the corrected positions nearly agreed with those of DEM1A, both at the beam level and at the footprint level with flow accumulation. (M1) and (M3) have the same model structure and differ only in the input. The low-resolution data synthesized from DEM1A are merely a coarsened version of the terrain information in DEM1A and do not contain the differences arising from different measurement methods that are contained in the real DTM pair. The input–output relationship therefore also differs between synthetic and real data, and this comparison alone cannot isolate the contribution of the model. On the other hand, the fact that the framework of this study gives nearly the same correction results as DEM1A when the input contains sufficient information means that improving the input DTM leads directly to improving the correction results.

6.5 Implications for super-resolution

The super-resolution results of this study also provide findings on the super-resolution of real data. First, the accuracy of the super-resolution trained and evaluated on synthetic data produced by coarsening DEM1A was far from that on real data. With synthetic data, the RMSE was less than 1 m even with bilinear interpolation, whereas with real data it is 3.80 m even after super-resolution. Wu et al. (2021) showed that a model trained on synthetic pairs of low- and high-resolution data does not even match interpolation on real data, and Panangian and Bittner (2024) also stated that super-resolution trained on synthetic data does not work on real data because real low-resolution data contain effects of sensors and acquisition conditions that interpolation cannot reproduce. The results of this study are consistent with these, and in addition, the conclusions on the footprint-level correction also differed between real and synthetic data. This shows that, when super-resolution is applied to downstream tasks, it must be trained and validated on real data. Second, the main factor that improved the super-resolution accuracy on real data was the fusion of the 30 m-resolution FABDEM, whose origin differs from that of the primary input. The same phenomenon was also reported by Cai and Wilson (2025), who increased the resolution of a global 30 m-resolution DEM by fusion with aerial images and other data and achieved an RMSE of about 1 m. However, the auxiliary inputs in these previous studies are optical images finer than the input, and they serve to restore details and to correct biases arising from ground objects (Argudo et al., 2018; Kubade et al., 2020; Cai and Wilson, 2025). The auxiliary input in this study is a DTM that is coarser than the input and of a different origin, and it reduced only the location-dependent bias without adding details. This confirms, within super-resolution, the finding from DEM fusion that fusing DEMs of different origins reduces error and bias (Okolie and Smit, 2022).

6.6 Significance and limitations

This study demonstrated that beam-level correction gives nearly the same results as DEM1A even with a super-resolved DTM, and gave one rough indication of the accuracy required for this. With the super-resolved reference DTM (RMSE 3.80 m), obtained by fusing a contour-derived 10 m-resolution DTM with a global 30 m-resolution DTM of a different origin, the beam-level offset agreed with that of DEM1A within 5 m for 84.9% of the beams. The accuracy of DTM-based geolocation correction of GEDI has so far been verified with DTMs of 0.5–1 m resolution (Tang et al., 2023; Schleich et al., 2023; Li et al., 2025; Tsutsumida et al., 2026), but the present results suggest that, even in areas where a DTM of roughly 10 m resolution is available, fusing it with a global DTM and super-resolving it to 1 m resolution may give beam-level corrections that are nearly the same as those obtained with a 1 m-resolution DTM. The requirement for the correction is that the reference-DTM error be small enough to be canceled out within a beam, and the bias is also required to be nearly 0. Beam-level correction may be usable for applications that use GEDI in units larger than a footprint, such as training data for wall-to-wall canopy height maps (Potapov et al., 2021; Lang et al., 2023) and grid-cell statistics, and it also serves as a preceding step for training methods that treat the geolocation error as constant within each track (Pauls et al., 2024).

However, there are two broad limitations to extending these results to other regions and conditions. The first is that the areas where a DTM with a resolution of around 10 m exists are also limited. In tropical and subtropical forested countries, either there is no free nationwide DTM or, where a nationwide DTM exists, it is derived from synthetic aperture radar or photogrammetry and affected by the canopy, and in some countries it is available only for a fee. Furthermore, training a super-resolution model requires 1 m-class training targets that can be transferred to the terrain of the target area, and within the GEDI coverage, the countries where a free 1 m-class DTM covers the whole country are limited to some countries in Western and Central Europe, the contiguous United States, New Zealand, and Japan. One way to solve this problem is to develop a 1 m-class super-resolution model that is transferable across the world and accepts an arbitrary input resolution at inference time. Several studies have addressed arbitrary input res-

olutions. He et al. (2022) demonstrated super-resolution that outputs elevation at an arbitrary upscaling factor by means of implicit neural representation. Their training targets were a 1 m-resolution LiDAR-derived DTM of Utah, USA, and a 2 m-resolution DTM of Slovenia, but the evaluation was limited to a comparison with interpolation in two areas totaling less than 100 km^2. On the other hand, Yao et al. (2024) used the same idea to make a single model handle upscaling factors from 2× to 8× and applied it to areas not used for training, but the resolutions of the training targets were 2 m, 10 m, and 30 m, and the training and evaluation were limited to mountainous areas of several hundred km^2, such as the Pyrenees and Tyrol. We found no study that trained and validated 1 m-class super-resolution on a global scale. The second is that the conditions under which the corrections agree have not been quantified. The indication was obtained with reference surfaces on a 1 m grid, and whether it applies to reference surfaces on coarser grids has not been verified. It is also a result obtained in forested areas that are steep by global standards and under the error distributions of the super-resolution and of the GEDI observed ground elevation, and it becomes stricter for beams with few footprints and for footprints with large errors in the GEDI ground elevation (Li et al., 2025). The influence is considered to be greater in areas with small relief; in areas where matching by elevation differences is hard to determine uniquely even with a 1 m-resolution DTM, matching would be very difficult with a super-resolved surface (Tang et al., 2023; Schleich et al., 2023). In addition, DTMs that differ from the GSI DTMs and FABDEM used as the input and training target in production method, data representation, or vertical datum may give different results.

7 Conclusion

This study examined, in steep forested areas of western Japan, whether a 1 m-resolution reference DTM generated by super-resolution from a 10 m-resolution DTM and an auxiliary DTM can substitute for a high-resolution DTM (DEM1A) in the geolocation correction of GEDI footprints. In the beam-level correction, the super-resolved reference DTM gave almost the same offsets as DEM1A, and the degree of agreement increased with the number of footprints in a beam. In the footprint-level correction, the super-resolved reference DTM did not reproduce the DEM1A-based corrected positions, and the corrected positions moved to locations where the elevation on DEM1A differs by the reference-DTM error.

This agreement in the beam-level correction is thought to have been obtained because the reference-DTM error cancels out among the footprints within a beam. Although how much of the error cancels out in an individual beam cannot be identified, beams that do not agree with DEM1A occur mostly among beams with few footprints, where the cancellation does not work, and the number of footprints in a beam serves as an indication of the reliability of the correction result. On the other hand, because the footprint-level correction tries to resolve the elevation difference with a single footprint alone, the corrected position is dominated by the error if the reference-DTM error is comparable to the elevation difference to be resolved. The reference DTM obtained in this study by super-resolving real data lacks the accuracy required for footprint-level correction, and footprint-level correction using it is not a substitute for footprint-level correction with DEM1A.

Most of the error of the super-resolution model in this study consists of components at scales that can be represented by a 10 m-resolution DTM and that remain even after averaging with the Gaussian window, and it is considered to originate mainly from the error originally present in the input. What the training could remove was the systematic error common to the whole area, and the elevation errors that vary from place to place could not be corrected with the input DTM alone. What reduced them and became the main factor in the accuracy improvement was the mid-fusion of FABDEM, whose origin differs from that of the primary input, but it does not sufficiently reduce the error at the scales of the 10 m-resolution DTM. Therefore, what is needed to obtain a super-resolution model that improves the correction accuracy is not the reproduction of fine relief but a substantial reduction of the error of the input DTM, and the addition of information sources of different origins and the use of optical images as an information source that explains the error of the input DTM are tasks for future work. In addition, the super-resolution accuracy obtained with synthetic data is not a substitute for the performance on real data, and super-resolution used for geolocation correction must be trained and validated on real data.

From the above, even without a 1 m-resolution DTM, fusing a DTM of roughly 10 m resolution with a global DTM and super-resolving it to 1 m resolution is considered to give beam-level corrections that are nearly the same as those obtained with a 1 m-resolution DTM. Given that the accuracy of DTM-based geolocation correction has so far been verified only with DTMs of 0.5–1 m resolution, this result extends the applicability of geolocation correction for applications that use GEDI in units larger than a footprint, as long as correction with a 1 m-resolution DTM is effective. However, the areas where both a 10 m-class DTM as the super-resolution input and a 1 m-class DTM as the training target are available are limited, and the conditions under which the correction results agree with those obtained with a 1 m-class DTM have not been quantified. To extend this method to areas without a 1 m-class DTM, the development of a super-resolution model that accepts an arbitrary input resolution and can be transferred to various regions is required, in addition to reducing the error of the input DTM.

Funding

This work was supported by JSPS KAKENHI Grant Numbers JP24K00244 and JP26K14728.

Acknowledgments

The 1 m and 10 m digital elevation models (DEM1A and DEM10B; Fundamental Geospatial Data, https://service.gsi.go.jp/kiban/app/) and the geoid model GSIGEO2011 (Ver. 2.2) were provided by the Geospatial Information Authority of Japan and were processed by the authors. FABDEM V1-2 (Neal and Hawker, 2023) was provided by the University of Bristol under the CC BY-NC-SA 4.0 license (https://creativecommons.org/licenses/by-nc-sa/4.0/). FABDEM is produced using Copernicus WorldDEM-30 © DLR e.V. 2010–2014 and © Airbus Defence and Space GmbH 2014–2018 provided under COPERNICUS by the European Union and ESA; all rights reserved. The organisations in charge of the Copernicus programme by law or by delegation do not incur any liability for any use of the Copernicus WorldDEM-30. GEDI L2A Version 2 data were obtained from the NASA Land Processes Distributed Active Archive Center (LP DAAC). The land use and land cover data used in this paper were provided by JAXA (High-Resolution Land Use and Land Cover Map of Japan, version 25.04). This paper uses the following works with modification: DCHM (Digital Canopy Height Model) 0.5 m, Hyogo Prefecture, and the Kochi Prefecture forest resource data (measured in 2018), both published through the G-spatial Information Center under CC BY 4.0.

Data and code availability

The code for reading the DTMs and FABDEM, for super-resolution, and for the geolocation correction, the trained weights of the super-resolution models, and the GEDI footprint positions before and after the correction with their observed elevations will be made publicly available on GitHub upon publication of the peer-reviewed version of this paper. The input data (GEDI L2A, FABDEM, the GSI digital elevation models, the JAXA land use and land cover map, and the DCHMs) are available from the providers listed in the Acknowledgments.

Declaration of competing interest

The authors declare that they have no known competing financial interests or personal relationships that could have appeared to influence the work reported in this paper.

Declaration of generative AI use

During the preparation of this work, the authors used Claude (Anthropic) through Claude Code to draft and translate text, to write and debug analysis code, and to typeset the manuscript. The authors reviewed and edited all output and take full responsibility for the content of this paper.

References

Adam, M., M. Urbazaev, C. Dubois, and C. Schmullius (2020). "Accuracy assessment of GEDI terrain elevation and canopy height estimates in European temperate forests: Influence of environmental and acquisition parameters". In: *Remote Sensing* 12.23, p. 3948. DOI: 10.3390/rs12233948.

Argudo, O., A. Chica, and C. Andujar (2018). "Terrain super-resolution through aerial imagery and fully convolutional networks". In: *Computer Graphics Forum: Journal of the European Association for Computer Graphics* 37.2, pp. 101–110. DOI: 10.1111/cgf.13345.

Cai, X. and M. D. Wilson (2025). "JSPSR: Joint Spatial Propagation Super-resolution networks for enhancement of bare-earth digital Elevation Models from global data". In: *Remote Sensing* 17.21, p. 3591. DOI: 10.3390/rs17213591.

Cardenas-Martinez, A., A. Pascual, E. Guisado-Pintado, and V. Rodriguez-Galiano (2025). "Using airborne LiDAR and enhanced-geolocated GEDI metrics to map structural traits over a Mediterranean forest". In: *Science of Remote Sensing* 11.100195, p. 100195. DOI: 10.1016/j.srs.2025.100195.

Corado, L., S. Godinho, C. A. Silva, A. Pascual, J. Guerra-Hernández, F. Valerio, T. Gonçalves, and P. Salgueiro (2026). "GEDICorrect: A scalable python tool for orbit-, beam-, and footprint-level GEDI geolocation correction". In: *Science of Remote Sensing* 14, p. 100469. DOI: 10.1016/j.srs.2026.100469.

Demiray, B. Z., M. Sit, and I. Demir (2021). "D-SRGAN: DEM super-resolution with generative adversarial networks". In: *SN Computer Science* 2.1. DOI: 10.1007/s42979-020-00442-2.

Dong, C., C. C. Loy, K. He, and X. Tang (2016). "Image super-resolution using deep convolutional networks". In: *IEEE Transactions on Pattern Analysis and Machine Intelligence* 38.2, pp. 295–307. DOI: 10.1109/TPAMI.2015.2439281.

Dubayah, R., J. Armston, S. P. Healey, J. M. Bruening, P. L. Patterson, J. R. Kellner, et al. (2022). "GEDI launches a new era of biomass inference from space". In: *Environmental research letters* 17.9, p. 095001. DOI: 10.1088/1748-9326/ac8694.

Dubayah, R., J. B. Blair, J. Beck, J. Armston, M. Hofton, and S. Luthcke (2026). *Global Ecosystem Dynamics Investigation (GEDI) Level 2 User Guide For SDPS PGEVersion 4 (P004) of GEDI L2A Data and SDPS PGEVersion 4 (P004) of GEDI L2B Data*. Tech. rep.

Dubayah, R., J. B. Blair, S. Goetz, L. Fatoyinbo, M. Hansen, S. Healey, et al. (2020). "The Global Ecosystem Dynamics Investigation: High-resolution laser ranging of the Earth's forests and topography". In: *Science of Remote Sensing* 1.100002, p. 100002. DOI: 10.1016/j.srs.2020.100002.

Farr, T. G., P. A. Rosen, E. Caro, R. Crippen, R. Duren, S. Hensley, et al. (2007). "The Shuttle Radar Topography Mission". In: *Reviews of Geophysics* 45.2. DOI: 10.1029/2005RG000183.

Grohmann, C. H., M. J. Smith, and C. Riccomini (2011). "Multiscale analysis of topographic surface roughness in the Midland Valley, Scotland". In: *IEEE Transactions on Geoscience and Remote Sensing* 49.4, pp. 1200–1213. DOI: 10.1109/TGRS.2010.2053546.

Hancock, S., J. Armston, M. Hofton, X. Sun, H. Tang, L. I. Duncanson, J. R. Kellner, and R. Dubayah (2019). "The GEDI simulator: A large-footprint waveform lidar simulator for calibration and validation of spaceborne missions". In: *Earth and Space Science* 6.2, pp. 294–310. DOI: 10.1029/2018EA000506.

Hawker, L., P. Uhe, L. Paulo, J. Sosa, J. Savage, C. Sampson, and J. Neal (2022). "A 30m global map of elevation with forests and buildings removed". In: *Environmental research letters*. DOI: 10.1088/1748-9326/ac4d4f.

He, P., Y. Cheng, M. Qi, Z. Cao, H. Zhang, S. Ma, S. Yao, and Q. Wang (2022). "Super-resolution of digital elevation model with local implicit function representation". In: *2022 International Conference on Machine Learning and Intelligent Systems Engineering (MLISE)*. IEEE, pp. 111–116. DOI: 10.1109/MLISE57402.2022.00030.

Helmy, M., E. Mandanici, L. Vittuari, and G. Bitelli (2026). "Super-resolving Digital Terrain Models using a modified RCAN". In: *Remote Sensing* 18.1, p. 20. DOI: 10.3390/rs18010020.

Hofton, M. A., J. B. Minster, and J. B. Blair (2000). "Decomposition of laser altimeter waveforms". In: *IEEE Transactions*

on Geoscience and Remote Sensing 38.4, pp. 1989–1996. DOI: 10.1109/36.851780.

Kim, J., J. K. Lee, and K. M. Lee (2016). "Accurate image super-resolution using very deep convolutional networks". In: *2016 IEEE Conference on Computer Vision and Pattern Recognition (CVPR)*. IEEE, pp. 1646–1654. DOI: 10.1109/CVPR.2016.182.

Kubade, A., D. Patel, A. Sharma, and K. S. Rajan (2020). "AFN: Attentional Feedback Network based 3D Terrain Super-Resolution". In: *Proceedings of the Asian Conference on Computer Vision*. DOI: 10.1007/978-3-030-69525-5_12.

Kutchartt, E., M. Pedron, and F. Pirotti (2022). "Assessment of canopy and ground height accuracy from gedi lidar over steep mountain areas". In: *ISPRS Annals of Photogrammetry Remote Sensing and Spatial Information Sciences* V-3-2022, pp. 431–438. DOI: 10.5194/isprs-annals-V-3-2022-431-2022.

Lang, N., W. Jetz, K. Schindler, and J. D. Wegner (2023). "A high-resolution canopy height model of the Earth". In: *Nature Ecology & Evolution* 7.11, pp. 1778–1789. DOI: 10.1038/s41559-023-02206-6.

Ledig, C., L. Theis, F. Huszar, J. Caballero, A. Cunningham, A. Acosta, et al. (2017). "Photo-realistic single image super-resolution using a generative adversarial network". In: *2017 IEEE Conference on Computer Vision and Pattern Recognition (CVPR)*. IEEE. DOI: 10.1109/cvpr.2017.19.

Li, H., X. Li, T. Hiroshima, T. Kato, and M. Hayashi (2025). "Improving GEDI geolocation accuracy with ultra-high-resolution DTM data in Japan". In: *GIScience & Remote Sensing* 62.1. DOI: 10.1080/15481603.2025.2601327.

Li, H., X. Li, T. Kato, M. Hayashi, J. Fu, and T. Hiroshima (2024). "Accuracy assessment of GEDI terrain elevation, canopy height, and aboveground biomass density estimates in Japanese artificial forests". In: *Science of Remote Sensing* 10.100144, p. 100144. DOI: 10.1016/j.srs.2024.100144.

Li, Z., X. Zhu, S. Yao, Y. Yue, Á. F. García-Fernández, E. G. Lim, and A. Levers (2023). "A large scale Digital Elevation Model super-resolution Transformer". In: *International Journal of Applied Earth Observation and Geoinformation: ITC Journal* 124.103496, p. 103496. DOI: 10.1016/j.jag.2023.103496.

Lim, B., S. Son, H. Kim, S. Nah, and K. M. Lee (2017). "Enhanced deep residual networks for single image super-resolution". In: *2017 IEEE Conference on Computer Vision and Pattern Recognition Workshops (CVPRW)*. IEEE. DOI: 10.1109/cvprw.2017.151.

Liu, A., X. Cheng, and Z. Chen (2021). "Performance evaluation of GEDI and ICESat-2 laser altimeter data for terrain and canopy height retrievals". In: *Remote Sensing of Environment* 264, p. 112571. DOI: 10.1016/j.rse.2021.112571.

Liu, W., Y. Zhong, S. Zhao, S. Luo, Y. Yu, X. Zhong, W. Tan, H. Guan, H. He, and J. Li (2026). "DEM super-resolution guided by high-resolution remote sensing images using multitask learning". In: *International Journal of Applied Earth Observation and Geoinformation: ITC Journal* 146.105099, p. 105099. DOI: 10.1016/j.jag.2026.105099.

Milenković, M., S. Schnell, J. Holmgren, C. Ressl, E. Lindberg, M. Hollaus, N. Pfeifer, and H. Olsson (2017). "Influence of footprint size and geolocation error on the precision of forest biomass estimates from space-borne waveform LiDAR". In: *Remote Sensing of Environment* 200, pp. 74–88. DOI: 10.1016/j.rse.2017.08.014.

Mkaouar, A., D. Shean, T. Yin, C. S. R. Neigh, R. V. Leite, P. M. Montesano, A. Kallel, and J.-P. Gastellu-Etchegorry (2025). "Refining satellite laser altimetry geolocation through full-waveform radiative transfer modeling and matching". In: *Science of Remote Sensing* 12.100248, p. 100248. DOI: 10.1016/j.srs.2025.100248.

Neal, J. and L. Hawker (2023). *FABDEM V1-2*. University of Bristol. Dataset. DOI: 10.5523/bris.s5hqmjcdj8yo2ibzi9b4ew3sn.

Okolie, C. J. and J. L. Smit (2022). "A systematic review and meta-analysis of Digital elevation model (DEM) fusion: pre-processing, methods and applications". In: *ISPRS Journal of Photogrammetry and Remote Sensing: Official Publication of the International Society for Photogrammetry and Remote Sensing (ISPRS)* 188, pp. 1–29. DOI: 10.1016/j.isprsjprs.2022.03.016.

Panangian, D. and K. Bittner (2024). "Real-GDSR: Real-world guided DSM super-resolution via edge-enhancing residual network". In: *ISPRS Annals of Photogrammetry Remote Sensing and Spatial Information Sciences* X-2-2024, pp. 185–192. DOI: 10.5194/isprs-annals-X-2-2024-185-2024.

Park, T., R. Kennedy, S. Choi, J. Wu, M. Lefsky, J. Bi, J. Mantooth, R. Myneni, and Y. Knyazikhin (2014). "Application of physically-based slope correction for maximum forest canopy height estimation using waveform lidar across different footprint sizes and locations: Tests on LVIS and GLAS". In: *Remote Sensing* 6.7, pp. 6566–6586. DOI: 10.3390/rs6076566.

Pauls, J., M. Zimmer, U. M. Kelly, M. Schwartz, S. Saatchi, P. Ciais, S. Pokutta, M. Brandt, and F. Gieseke (2024). "Estimating Canopy Height at Scale". In: *International Conference on Machine Learning*. PMLR, pp. 39972–39988.

Pavlis, N. K., S. A. Holmes, S. C. Kenyon, and J. K. Factor (2012). "The development and evaluation of the Earth Gravitational Model 2008 (EGM2008)". In: *Journal of Geophysical Research* 117.B4. DOI: 10.1029/2011JB008916.

Potapov, P., X. Li, A. Hernandez-Serna, A. Tyukavina, M. C. Hansen, A. Kommareddy, et al. (2021). "Mapping global forest canopy height through integration of GEDI and Landsat data". In: *Remote Sensing of Environment* 253.112165, p. 112165. DOI: 10.1016/j.rse.2020.112165.

Quiros, E., M.-E. Polo, and L. Fragoso-Campon (2021). "GEDI elevation accuracy assessment: A case study of southwest Spain". In: *IEEE Journal of Selected Topics in Applied Earth Observations and Remote Sensing* 14, pp. 5285–5299. DOI: 10.1109/JSTARS.2021.3080711.

Roy, D. P., H. B. Kashongwe, and J. Armston (2021). "The impact of geolocation uncertainty on GEDI tropical forest canopy height estimation and change monitoring". In: *Science of Remote Sensing* 4.100024, p. 100024. DOI: 10.1016/j.srs.2021.100024.

Schleich, A., S. Durrieu, M. Soma, and C. Vega (2023). "Improving GEDI footprint geolocation using a high-resolution digital elevation model". In: *IEEE Journal of Selected Topics in Applied Earth Observations and Remote Sensing* 16, pp. 7718–7732. DOI: 10.1109/JSTARS.2023.3298991.

Shannon, E. S., A. O. Finley, D. J. Hayes, S. N. Noralez, A. R. Weiskittel, B. D. Cook, and C. Babcock (2024). "Quantifying and correcting geolocation error in spaceborne LiDAR forest canopy observations using high spatial accuracy data: A Bayesian model approach". In: *Environmetrics* 35.4, e2840. DOI: 10.1002/env.2840.

Tang, H., J. Stoker, S. Luthcke, J. Armston, K. Lee, B. Blair, and M. Hofton (2023). "Evaluating and mitigating the impact of systematic geolocation error on canopy height measurement performance of GEDI". In: *Remote Sensing of Environment* 291.113571, p. 113571. DOI: 10.1016/j.rse.2023.113571.

Tsutsumida, N., R. Mitsuhashi, Y. Sawada, and A. Kato (2026). "SALPA: Spaceborne LiDAR point adjustment for enhanced footprints geolocation". In: *Science of Remote Sensing* 14, p. 100515. DOI: 10.1016/j.srs.2026.100515.

Wang, H., L. Xiong, G. Hu, H. Cao, S. Li, G. Tang, and L. Zhou (2024). "DEM super-resolution framework based on deep learning: decomposing terrain trends and residuals". In: *International Journal of Digital Earth* 17.1. DOI: 10.1080/17538947.2024.2356121.

Wang, X., R. Wang, B. Yang, L. Yang, F. Liu, and K. Xiong (2025). "Simulation-based correction of geolocation errors in GEDI footprint positions using Monte Carlo approach". In: *Forests* 16.5, p. 768. DOI: 10.3390/f16050768.

Wu, Z., Z. Zhao, P. Ma, and B. Huang (2021). "Real-world DEM super-resolution based on generative adversarial networks for improving InSAR topographic phase simulation". In: *IEEE Journal of Selected Topics in Applied Earth Observations and Remote Sensing* 14, pp. 8373–8385. DOI: 10.1109/JSTARS.2021.3105123.

Xu, Y., S. Ding, P. Chen, H. Tang, H. Ren, and H. Huang (2023). "Horizontal geolocation error evaluation and correction on full-waveform LiDAR footprints via waveform matching". In: *Remote Sensing* 15.3, p. 776. DOI: 10.3390/rs15030776.

Yang, C., D. Peng, K. Deng, L. Jiang, M. Zhao, W. Zeng, Y. Shao, and N. Wang (2024). "Quantification of GEDI geolocation error and its influence on elevation and canopy height". In: *IEEE Journal of Selected Topics in Applied Earth Observations and Remote Sensing* 17, pp. 18012–18024. DOI: 10.1109/JSTARS.2024.3461843.

Yao, S., Y. Cheng, F. Yang, and M. G. Mozerov (2024). "A continuous digital elevation representation model for DEM super-resolution". In: *ISPRS Journal of Photogrammetry and Remote Sensing: Official Publication of the International Society for Photogrammetry and Remote Sensing (ISPRS)* 208, pp. 1–13. DOI: 10.1016/j.isprsjprs.2024.01.001.

Yu, J., Y. Li, X. Bai, R. Yang, M. Cui, H. Wu, et al. (2025). "A DEM super resolution reconstruction method based on normalizing flow". In: *Scientific Reports* 15.1, p. 10681. DOI: 10.1038/s41598-025-94274-w.

Zhang, Y. and W. Yu (2022). "Comparison of DEM super-resolution methods based on interpolation and neural networks". In: *Sensors* 22.3, p. 745. DOI: 10.3390/s22030745.

Zhang, Y., W. Yu, and D. Zhu (2022). "Terrain feature-aware deep learning network for digital elevation model superresolution". In: *ISPRS Journal of Photogrammetry and Remote Sensing: Official Publication of the International Society for Photogrammetry and Remote Sensing (ISPRS)* 189, pp. 143–162. DOI: 10.1016/j.isprsjprs.2022.04.028.

Zhang, Y., K. Li, K. Li, L. Wang, B. Zhong, and Y. Fu (2018). "Image super-resolution using very deep residual channel attention networks". In: *Computer Vision – ECCV 2018*. Lecture Notes in Computer Science. Cham: Springer International Publishing, pp. 294–310. DOI: 10.1007/978-3-030-01234-2_18.

Zheng, X., Z. Bao, and Q. Yin (2023). "Terrain self-similarity-based transformer for generating super resolution DEMs". In: *Remote Sensing* 15.7, p. 1954. DOI: 10.3390/rs15071954.

Zheng, X., Z. Xu, Q. Yin, Z. Bao, Z. Chen, and S. Wang (2024). "A Transformer-Unet Generative Adversarial Network for the super-resolution reconstruction of DEMs". In: *Remote Sensing* 16.19, p. 3676. DOI: 10.3390/rs16193676.